

# Exploring the Dust Content of Galactic Winds with *Herschel*.

## I. NGC 4631<sup>1</sup>

M. Meléndez<sup>1</sup>, S. Veilleux<sup>1,2</sup>, C. Martin<sup>3</sup>, C. Engelbracht<sup>4</sup>, J. Bland-Hawthorn<sup>5</sup>, G. Cecil<sup>6</sup>, F. Heitsch<sup>6</sup>, A. McCormick<sup>1</sup>, T. Müller<sup>7</sup>, D. Rupke<sup>8</sup> & S. H. Teng<sup>9</sup>

### ABSTRACT

We present a detailed analysis of deep far-infrared observations of the nearby edge-on star-forming galaxy NGC 4631 obtained with the *Herschel Space Observatory*. Our PACS images at 70 and 160  $\mu\text{m}$  show a rich complex of filaments and chimney-like features that extends up to a projected distance of 6 kpc above the plane of the galaxy. The PACS features often match extraplanar  $\text{H}\alpha$ , radio-continuum, and soft X-ray features observed in this galaxy, pointing to a tight disk-halo connection regulated by star formation. On the other hand, the morphology of the colder dust component detected on larger scale in the SPIRE 250, 350, and 500  $\mu\text{m}$  data matches the extraplanar H I streams previously reported in NGC 4631 and suggests a tidal origin. The PACS 70/160  $\mu\text{m}$  ratios are elevated in the central  $\sim 3.0$  kpc region above the nucleus of this galaxy (the “superbubble”). A pixel-by-pixel analysis shows that dust in this region has a higher temperature and/or an emissivity with a steeper spectral index ( $\beta > 2$ ) than the dust in the disk, possibly the result of the harsher environment in the superbubble. Star formation in the disk seems energetically insufficient to lift the material out of the disk, unless it was more active in the past or the dust-to-gas ratio in the superbubble region is higher than the Galactic value. Some of the dust in the halo may also have been tidally stripped from nearby companions or lifted from the disk by galaxy interactions.

---

<sup>1</sup>Department of Astronomy, University of Maryland, College Park, MD 20742, USA; marcio@astro.umd.edu, veilleux@astro.umd.edu

<sup>2</sup>Joint Space-Science Institute, University of Maryland, College Park, MD 20742, USA

<sup>3</sup>Department of Physics, University of California, Santa Barbara, CA 93106

<sup>4</sup>Department of Astronomy, University of Arizona, Tucson, Arizona 85721 (deceased)

<sup>5</sup>Department of Physics, University of Sydney, Sydney, NSW 2006, Australia

<sup>6</sup>Department of Physics, University of North Carolina, Chapel Hill, NC 27599

<sup>7</sup>Max-Planck-Institute for Extraterrestrial Physics (MPE), Giessenbachstraße 1, 85748 Garching, Germany

<sup>8</sup>Department of Physics, Rhodes College, Memphis, TN 38112

<sup>9</sup>Science and Tech Division, Institute for Defense Analyses, Alexandria, VA 22311

<sup>1</sup>*Herschel* is an ESA space observatory with science instruments provided by European-led Principal Investigator consortia and with important participation from NASA.

## 1. Introduction

The interstellar medium (ISM) of galaxies keeps a record of one of their most important properties: their star formation history. As galaxies age, their dying stars enrich the ISM by injecting gas and dust that eventually make up the next generation of stars. As a consequence of this recycling process, interstellar dust plays a fundamental role in the chemistry and appearance of a galaxy. Dust grains are unambiguously associated with galaxy evolution because they can work as a catalyst for chemical reactions resulting in the creation of molecules, they can absorb and re-emit starlight thus helping with the heating and cooling of the ISM, and they can remove heavy elements from the gas phase. For all these reasons, it is crucial to understand the location and dust content of galaxies in order to understand galaxy evolution. In this regard, galactic winds are the primary mechanism in which gas and dust can be recycled through the entire galaxy. Thus, it is important to study the geometry, mass, and energy of dusty galactic winds (see Veilleux et al. 2005, for a review). Overall, dusty galactic winds can have a direct impact on the morphology of the galaxy and could be a leading factor in regulating the star formation rate (SFR) by removing the material from which stars are formed (Roussel et al. 2010; Bolatto et al. 2013; Sturm et al. 2011; Veilleux et al. 2013; Cicone et al. 2014).

This first paper in a series focuses on the nearby (7.4 Mpc, Radburn-Smith et al. 2011), edge-on ( $i \sim 86^\circ$ ) starburst galaxy, NGC 4631. This galaxy shows a prominent multi-phase halo that comprises a relativistic radio component (Ekers & Sancisi 1977; Hummel et al. 1988; Hummel & Dettmar 1990), diffuse ionized gas (Rand et al. 1992; Donahue et al. 1995; Golla et al. 1996; Hoopes et al. 1999), dust (Martin & Kern 2001), molecular gas (Rand 2000; Irwin et al. 2011), and hot X-ray emitting plasma (Fabbiano & Trinchieri 1987; Wang et al. 1995; Vogler & Pietsch 1996; Wang et al. 2001; Strickland et al. 2004; Tüllmann et al. 2006b; Yamasaki et al. 2009). The dimension (vertical height) of the halo ranges from 740 pc (molecular gas; Rand 2000) up to 18 kpc (ionized gas; Donahue et al. 1995). This object thus offers an unique opportunity to study the connection between the disk and the extended emission in galaxies. Galactic-scale winds or outflows may be responsible for ejecting the dusty gas from the disk into the halo (e.g., Golla & Hummel 1994) and, ultimately, heating and enriching the circumgalactic medium. There has been mounting evidence for this outflowing gas in NGC 4631 (Hummel & Dettmar 1990; Golla & Hummel 1994; Alton et al. 1999; Hoopes et al. 1999; Rand 2000; Israel 2009; Irwin et al. 2011), thus the question: what powers this outflow? Given the fact that there is no active galactic nucleus in the center of NGC 4631, a starburst-driven wind seems appropriate. Contrary to M82 (Lynds & Sandage 1963; Alton et al. 1999), NGC 4631 does not possess a nuclear starburst, but rather a central molecular ring (Dumke et al. 2001; Irwin et al. 2011) with widespread  $H\alpha$  and UV emission distributed throughout the entire stellar disk (Crillon & Monnet 1969; Rand et al. 1992; Smith et al. 2001). Galaxy interactions may also have played a role in shaping the gaseous halo. NGC 4631 lives in a group which has been extensively studied in H I 21-cm, where tidal spurs and two highly energetic supershells have been detected (Roberts 1968; Weliachew et al. 1978; Combes 1978; Rand & van der Hulst 1993; Rand 1994). NGC 4627, a dwarf elliptical galaxy ( $\sim 3'$  NW of the nucleus), and NGC 4656, an edge-on

spiral ( $\sim 30'$  SE of the nucleus), are the most prominent companion galaxies of NGC 4631. The NGC 4631 group of galaxies also contains three dwarfs observed in H I (Rand & van der Hulst 1993; Rand 1994), a young optical dwarf galaxy candidate (Seth et al. 2005a), and an UV-bright tidal dwarf galaxy (Schechtman-Rook & Hess 2012).

There is also some evidence for dust outside the main body of the galaxy. The first detection of a cold dust component in NGC 4631 was presented by Braine et al. (1995) at 1.3 mm where they found a good correspondence between the CO (Golla & Wielebinski 1994) and the 1.3 mm continuum in the inner 2 kpc of the galaxy. A deeper map presented by Neininger & Dumke (1999) proved the existence of a cold dust component at 1.2 mm outside the disk of the galaxy that follows (in part) the more extended H I extraplanar emission. The first maps at 450 and 850  $\mu\text{m}$  were presented by Alton et al. (1999), focusing on the inner  $3'$  where they tentatively connected the expulsion of dust grains (dust outflow) with various small “chimneys” or extraplanar dusty filaments associated with the enhanced and widespread star formation activity in NGC 4631. Far-infrared (FIR) and submillimeter maps and fluxes for NGC 4631 can be found in various studies including, Bendo et al. (2003, 2006), Dumke et al. (2004), Dale et al. (2005, 2007, 2009) and Stevens et al. (2005). However, despite the great effort to understand the warm dust properties and structure in NGC 4631, all the previous studies were limited by relatively poor angular resolution. The superior angular resolution and sensitivity of *Herschel Space Observatory* (Pilbratt et al. 2010) provides an unique opportunity to study the dust content and structure of nearby galaxies.

In this paper we present a spatially resolved analysis of the warm-to-cold dust components in NGC 4631 using our own *Herschel* observations at 70, 100, 160, 250, 350, and 500  $\mu\text{m}$ . This paper is structured as follows. In Section 2, we describe in detail the different *Herschel* observations used in our analysis and the data processing. In Section 3, we present a morphological comparison between the *Herschel* observations and published data spanning the entire radio to X-ray energy range in order to investigate the connection between the various components in the halo. Section 4 presents the results from a more detailed analysis of our data, including the dust temperature morphology of the warm and cold dust components in the halo (Section 4.1 and 4.2), dust mass estimates (Section 4.3), star formation rates (Section 4.4), and a spatially resolved dust analysis of NGC 4631 (Section 4.5). In Section 5 we develop a picture for the origin and properties of the dusty halo in NGC 4631. Finally, the main conclusions are summarized in Section 6. In addition, Appendix A presents a detailed comparison between the FIR flux and color maps and the brightest X-ray point sources detected in this galaxy with *Chandra*. Throughout this paper, we adopt a distance of 7.4 Mpc for NGC 4631 (Radburn-Smith et al. 2011), corresponding to a linear scale of  $\sim 36$  pc per arcsecond.

## 2. Observations and Data Processing

NGC 4631 was observed with the Photodetector Array Camera and Spectrometer (PACS, Poglitsch et al. 2010) on board *Herschel*. The main observations presented in this work are from

our cycle 1 open-time program (OT1\_sveilleu.2, PI: S. Veilleux). For this program we obtained simultaneous PACS imaging for the PACS blue  $70\ \mu\text{m}$  ( $60\text{--}85\ \mu\text{m}$ ) and red  $160\ \mu\text{m}$  ( $130\text{--}210\ \mu\text{m}$ ) channels in scan mode along seven position angles at  $50^\circ$ ,  $60^\circ$ ,  $70^\circ$ ,  $110^\circ$ ,  $120^\circ$ ,  $130^\circ$ , and  $140^\circ$  (Obs IDs: 1342235130, 1342235131, 1342235132, 1342235133, 1342235134, 1342235135 and 1342235136). At each orientation angle, we requested 76 scan legs of  $6.0'$  length,  $4.0''$  scan leg separation, a repetition factor of two, and a scan speed of  $20''\ \text{s}^{-1}$ . The total time per position angle, including telescope overhead, was  $\sim 1.6$  hours, for a total request of 11.1 hours. We complement our program with archival observations at 70, 100 and  $160\ \mu\text{m}$  obtained from the “Key Insight of Nearby Galaxies: A Far-Infrared Survey with Herschel” (KINGFISH) open-time key program (KPOT\_rkennicu\_1). These observations were taken in scan mode along two position angles at  $45^\circ$  and  $135^\circ$  (Obs IDs: 1342209672, 1342209673, 1342209674 and 1342209675). At each orientation angle, the observations consisted of one scan leg of  $21.0'$  length,  $2.0''$  scan leg separation, a repetition factor of three, obtained at a scan speed of  $20''\ \text{s}^{-1}$ . The total observation time per scan angle, including telescope overhead, was  $\sim 0.7$  hours, for a total of  $\sim 1.4$  hours. Observations from the Spectral and Photometric Imaging Receiver (SPIRE, Griffin et al. 2010) were taken simultaneously at 250, 350, and  $500\ \mu\text{m}$  as part of the KINGFISH open-time key program. NGC 4631 was observed in large map mode covering an area of  $23' \times 23'$  with two repetitions at nominal speed ( $30''\ \text{s}^{-1}$ ).

For the PACS data reduction, we used the Herschel Interactive Processing Environment (HIPE, Ott 2010) version 8.0. The “Level 0” observations (raw data) were processed through the standard pipeline procedure to convert from Level 0 to Level 1 data. This procedure includes the extraction of the calibration tree needed for the data processing, correction for electronic crosstalk, application of the flat-field correction, and finally deglitching and conversion from Volts to janskys per array pixel. In order to correct for bolometer drift (low frequency noise), both thermal and non-thermal (uncorrelated noise), and to create the final maps from the Level 1 data, we used the algorithm implemented in *Scanamorphos* (v21.0, Roussel 2013), which makes use of the redundancy built in the observations to derive the brightness drifts. Because of this, *Scanamorphos* is independent of any pre-defined noise model because it relies on the fact that each portion of the sky is scanned by multiple bolometers at different times. All final PACS maps have a pixel size of  $\sim 1/4$  of the PSF FWHM, i.e.,  $1.4''$  at  $70\ \mu\text{m}$  and  $2.85''$  at  $160\ \mu\text{m}$ . *Scanamorphos* also produces error and weight maps. The error map is defined as the error on the mean brightness in each pixel. It is built using the weighted variance because weights are used for the projection of the final map. The error map does not include any error propagation associated with the different steps performed on the pipeline. On the other hand, the weighted map is built by co-adding the weights and is normalized by the average of the weights. Given the relatively small field of view of our observations, relative to the size of the galaxy, and the observing strategy, we created the *Scanamorphos* maps with the “minimap” and “flat” options. On the other hand, the SPIRE data was processed from “level 0” up to level 1 with the HIPE scripts included in the *Scanamorphos* distribution. The preprocessing by the pipeline includes the same steps as in the PACS pipeline except that the conversion to brightness is in janskys per beam and the thermal drifts are subtracted by using the smoothed series of thermistors located on the detector array as the input of the drift model (see Ott 2010,

for details). The final SPIRE maps have a pixel size of  $\sim 1/4$  of the PSF FWHM, i.e.,  $4.5''$ ,  $6.25''$ , and  $9.0''$  at 250, 350, and 500  $\mu\text{m}$ , respectively.

To extract the global fluxes, we chose an elliptical aperture that visually encloses all of the observed emission at 500  $\mu\text{m}$ . The parameters of this ellipse are: major and minor semi-axes of 514 and  $150''$ , and position angle of  $84^\circ$ , measured anti-clockwise from north to east (i.e. aligned along the major axis of the disk). In addition, background subtraction is performed locally with a circular or elliptical annulus around the source where the background annulus was set to encompass a clean, uncontaminated sky region close to the source. For the large field of view observations (KPOT\_rkennicu\_1), the background contribution is measured in an elliptical annulus with inner major and minor semi-axis equal to the global flux aperture and outer major and minor axis equal to 1.2 times the inner values. For the smaller field of view observations (70 and 160  $\mu\text{m}$ , OT1\_sveilleu\_2), where the global elliptical aperture is larger than the field of view, the sky background (and standard deviation) was measured from 10 circular apertures placed above and below the galaxy plane, not too close to the galaxy (to avoid galaxy contamination) and far from the edges of the map (to avoid unreliable fluxes due to elevated noise). The total uncertainty on the integrated photometric measurements is a combination of the error on the mean brightness in each pixel added in quadrature within the source aperture (the error map produced by *Scanamorphos*), the standard deviation of all the pixels in the background aperture, and the PACS photometer flux calibration accuracy. For the calibration uncertainties (extended sources), we adopted a large (conservative) value of 10% for both PACS and SPIRE. This value comes from adding the systematic (4-5%), statistical (1-2%), and PSF/beam size uncertainties (4%). To derive aperture corrections, we used the higher resolution image from *Spitzer*/IRAC 8.0  $\mu\text{m}$  (McCormick et al. 2013) and measured the total flux with the same aperture employed for our analysis. Then we convolved the same image with the appropriate kernel to bring it to the PACS resolution<sup>2</sup> (Aniano et al. 2011) and remeasured the flux in the same aperture. The ratio of the unconvolved to the convolved (the same PSF as the *Herschel* PACS) flux is used as an estimate of the aperture correction. For the global flux, the big aperture resulted in small corrections with values of 1.01, 1.01, and 1.02 for PACS 70, 100, and 160  $\mu\text{m}$ , respectively, and 1.00 for all of the SPIRE images. We color-corrected PACS fluxes assuming a modified blackbody with  $\beta = 2$  and a blackbody temperature of  $T = 30$  K ( $0.977/0.974/1.037$  at 70/100/160  $\mu\text{m}$ )<sup>3</sup>.

Our PACS flux densities for the entire galaxy are  $141.9 \pm 14.2$ ,  $232.9 \pm 23.3$ , and  $247.0 \pm 24.7$  Jy at 70, 100, and 160  $\mu\text{m}$ , respectively (see Table 1). These fluxes are consistent, within the uncertainties, with the (color uncorrected) *Herschel* fluxes from (Dale et al. 2012,  $137 \pm 7$ ,  $223 \pm 11$ , and  $246 \pm 12$  at 70, 100, and 160  $\mu\text{m}$ , respectively). Our values are also in agreement with the *Spitzer* MIPS photometry of NGC 4631 presented by (Dale et al. 2009,  $138 \pm 17$  and  $269 \pm 42$  Jy at

---

<sup>2</sup><http://www.astro.princeton.edu/~ganiano/Kernels.html>

<sup>3</sup>PACS Photometer Passbands and Colour Correction Factors for Various Source SEDs. Document PICC-ME-TN-038, version 1.0

70 and 160  $\mu\text{m}$ , respectively). In addition, there are reported values for the (color-corrected) *IRAS* total flux densities at 60 and 100  $\mu\text{m}$  of  $89.3 \pm 13.4$  Jy and  $216.4 \pm 32.5$  Jy from Rice et al. (1988), and  $90.7 \pm 18.2$  and  $170.4 \pm 34.1$  at 60 and 100  $\mu\text{m}$ , respectively (Young et al. 1989). To convert the SPIRE data from  $\text{Jy beam}^{-1}$  to  $\text{Jy pixel}^{-1}$ , we used the pipeline beam area as provided in the SPIRE Data Reduction Guide, Table 6.7, i.e., 465.39, 822.58, and 1768.66  $\text{arcsec}^2$  at 250, 350, and 500  $\mu\text{m}$ , respectively. For the SPIRE fluxes, we applied color corrections for extended sources assuming a gray body with emissivity index  $\beta = 2.0$  and modified blackbody temperature of 30 K (0.9790/0.9687/0.9783 at 250/350/500  $\mu\text{m}$ )<sup>4</sup>. The parameters used for the PACS and SPIRE color corrections are based on our full analysis of the spectral energy distribution of NGC 4631 (see Section 4.3). Our SPIRE global flux densities are  $111.4 \pm 11.1$ ,  $50.0 \pm 5.0$ , and  $19.9 \pm 2.0$  Jy at 250, 350, and 500  $\mu\text{m}$ , respectively. Our SPIRE fluxes are consistent, within the uncertainties, with the (color-uncorrected) *Herschel* fluxes from (Dale et al. 2012, with  $124 \pm 9$ ,  $54.5 \pm 3.9$ , and  $24.0 \pm 1.7$  Jy at 250, 350, and 500  $\mu\text{m}$ , respectively).<sup>5</sup>

### 3. Morphological Comparisons with Ancillary Data Sets

In addition to the PACS and SPIRE observations, we assembled a set of multi-wavelength ancillary observations for the purpose of multiphase comparisons. In the mid-infrared, we used images from *Spitzer* IRAC 4.5 and 8  $\mu\text{m}$  and MIPS 24  $\mu\text{m}$  (Dale et al. 2009; McCormick et al. 2013). In the optical, we compared the *Herschel* data with observations of the warm ionized gas in  $\text{H}\alpha$  (Rand et al. 1992), and in the radio, we used the atomic hydrogen  $\text{H I}$  21 cm maps of (Rand 1994) and the *L*-band (1.5 GHz) images from Irwin et al. (2012). Finally we also compared the *Herschel* data with soft X-ray images (0.3 – 2.0 keV) from our own analysis of archival *Chandra* observations of NGC 4631, where the final image was created following the procedure described in Strickland et al. (2004). For these comparisons, we enhanced the fainter features in our PACS and SPIRE images by using the adaptive median smoothing code ADAPTSMOOTH with a minimum signal-to-noise ratio (S/N) equal to 10 per pixel with a direct local noise estimate (version V.2.7.1.15.11.2010, Zibetti 2009; Zibetti et al. 2009). This adaptive smoothing scheme retains the image effective resolution and does not alter the photometric fluxes.

The results of the comparisons with the *Spitzer* data are shown in Figure 1. Note that the closest companion galaxy, NGC 4627, is not detected in any of the *Herschel* maps, not even in our very deep PACS images whereas it is clearly detected in the IRAC maps at 4.5 and 8  $\mu\text{m}$ . This result indicates that NGC 4627 is highly depleted in (warm and cold) dust, consistent with its classification as a dwarf elliptical galaxy.

---

<sup>4</sup>Table 5.7 in SPIRE Handbook, version 2.5, March 17, 2014

<sup>5</sup>Note that the SPIRE fluxes presented in Dale et al. (2012) were estimated with a different set of beam areas than the ones used in the present work, namely, 423, 751, and 1587  $\text{arcsec}^2$  at 250, 350, and 500  $\mu\text{m}$ .

In Figure 2 we present the comparison between the PACS images at 70 and 160  $\mu\text{m}$  and the diffuse ionized gas in  $\text{H}\alpha$  (see Rand et al. 1992, for details of the observations). The  $\text{H}\alpha$  image shows a rich complex of filaments and worm-like structures extending vertically from the disk of the galaxy. These structures coincide in position with similar structures in our deep exposure PACS images and high angular resolution C-band (6 GHz) images (Irwin et al. 2012), suggesting the existence of a close connection, *via* star formation, between the dust, the relativistic plasma, and the warm ionized gas (e.g., Cooper et al. 2008). This match is particular good above the center of the galaxy: Figure 3 shows a close-up comparison of the central region of NGC 4631 between our PACS observations at 70  $\mu\text{m}$  and  $\text{H}\alpha$ . Near the center of the galaxy, two worm-like structures can be seen extending above the northern edge of the  $\text{H}\alpha$  (below label “A”, Rand et al. 1992). This double-worm structure can also be seen in the PACS image at 70  $\mu\text{m}$ . This structure has been associated in the past with the breakout of a superbubble produced by a nuclear star formation event, but not a starburst (Rand et al. 1992). In addition, this split  $\text{H}\alpha$  filament appears to be associated with strong diffuse X-ray emission and two radio plumes of similar size. Wang et al. (1995) have suggested that magnetic pressure plays a role in confining the hot gas bubble above the plane of the galaxy.

To look further into this issue, we compare the smoothed PACS images with the 1.5 GHz and soft X-ray data in Figure 4. We find a good match between the FIR, radio and soft X-ray morphological features. In this comparison, the X-ray contours are from the soft X-ray (0.3-2.0 keV) *Chandra* observations whereas the radio contours show the 1.5 GHz image as obtained from Irwin et al. (2012). While the agreement is more evident in the bright disk of the galaxy, it is also seen in the halo at fainter flux levels. Note the loop-like feature  $\sim 5$  kpc north and east of the galaxy’s major axis in the PACS images. This extraplanar structure is enhanced in our smoothed maps and it is co-located with a large radio loop at 1.5 GHz (Irwin et al. 2012) and a similar soft X-ray loop, interior to the bigger radio continuum loop. Given the fact that the X-ray loop is interior to the radio loop, Irwin et al. (2012) suggested that the hot X-ray emitting plasma is confined by magnetic pressure. In a similar way, the FIR loops is slightly smaller than the radio loop, but a better match with the soft X-ray loop. Magnetic pressure confinement may therefore also influence the warm dust component in this region. Finally, note in Figure 4 the FIR emission extending towards the south at the eastern end of the disk, in direction of the companion, NGC 4656.

Next, in order to test the connection between the cold dust and gas, we compare our SPIRE observations with those from atomic hydrogen, H I 21-cm emission (see Rand 1994, for details of the observations and data processing). Figure 5 shows the H I gas as a contour plot with  $45'' \times 87''$  resolution overlaid on the SPIRE 250, 350, and 500  $\mu\text{m}$  images. For this comparison, we labeled four H I tidal spurs, following the nomenclature of Weliachew et al. (1978). Figure 5 shows that Spur 4 is also detected in the SPIRE bands, especially at 250  $\mu\text{m}$ . This result suggests that Spur 4 can be traced back to emission from the disk, as first proposed by Rand (1994). A similar correspondence was found between the extraplanar cold dust distribution at 1.2 mm and H I 21-cm (Neininger & Dumke 1999). Note that the magnetic field orientation in this region (north-east

of the galaxy center) also seems to be aligned with Spur 4 and the cold dust component (Golla & Hummel 1994; Mora & Krause 2013). On the other hand, there is no match between the cold gas and dust in Spur 3, suggesting that there is no gas and dust associated with NGC 4627 (at the sensitivity of the H I and SPIRE observations). Note that numerical simulations of the tidal interactions within the NGC 4631 group of galaxies require NGC 4627 as a source of gas in the past to create Spurs 2 and 3 (Combes 1978).

## 4. Results

### 4.1. PACS Colors

Typically, the FIR emission from galaxies peaks between  $\sim 70$  and  $\sim 160$   $\mu\text{m}$ . Given our deep PACS 70 and 160  $\mu\text{m}$  images, the  $S_{70}/S_{160}$  ratio can be used as a stand-alone color diagnostic to provide useful information on the peak of the FIR spectral energy distribution (SED), a proxy for the dust temperature and the dust properties. Figure 6 compares the  $S_{70}/S_{160}$  ratio map with the X-ray and radio emission (shown as contours) in NGC 4631. For this comparison, we convolved the 70  $\mu\text{m}$  map to the PACS kernel at 160  $\mu\text{m}$  (Aniano et al. 2011) and then applied the adaptive median smoothing code ADAPTSMOOTH with a S/N = 10 per pixel with a direct local noise estimate. Thus, the resulting  $S_{70}/S_{160}$  ratio image has a  $2.85''$   $\text{pixel}^{-1}$  resolution, corresponding to the resolution of the PACS 160  $\mu\text{m}$  *Scanamorphos* map. Note that at this scale each pixel in the ratio map is not independent of its neighbors. However, this map can be used to look for relative changes in temperature and dust properties independent of any modeling.

The upper panel of Figure 6 nicely shows the extent of the dusty halo in NGC 4631 and the existence of a warm central structure extending up to 6 kpc north of the major axis of the galaxy. This structure (hereafter called “superbubble” to distinguish it from smaller bubble-like structures seen in the disk) appears to be partially enclosed by the dusty, giant arch observed by Neininger & Dumke (1999) in the 1.2 mm cold-dust continuum emission. However, this cold arch is not a single structure but a projection between the tidal H I Spur 4 and an H I plume extending up from the disk (Taylor & Wang 2003). This result emphasizes that caution must be taken with any visual interpretation of the data as projection effects may confuse the picture. The southern edge of the superbubble coincides with the location of the nuclear double-worm structure observed in the H $\alpha$  and PACS 70  $\mu\text{m}$  maps (see Figure 3), suggesting a chimney mode that ejects hot dust out of the disk into the halo along the magnetic field lines (Hummel et al. 1991; Irwin et al. 2012; Mora & Krause 2013). In addition, the superbubble seems to coincide with a large shell of emission or loop observed in the H $\alpha$  + [N II] image of NGC 4631, extending 3.7 kpc into the halo (we adjust the size of the loop by our adopted distance, Hoopes et al. 1999). The lower panels of Figure 6 show a good correspondence between the far-infrared ratios and the soft X-ray (0.3 – 2.0 keV) and radio (1.5 GHz) emission, reinforcing the idea of a physical link between the hot and relativistic gas phases and the warm dust above the disk of the galaxy.



The upper panel of Figure 6 also shows the position and size of the two expanding H I supershells found by Rand & van der Hulst (1993) in the disk of NGC 4631. It can be seen that the positions of both supershells coincide with luminous X-ray sources and prominent regions of star formation (discussed in Appendix A). Higher dust temperatures (higher  $S_{70}/S_{160}$  values) are also seen near these positions, especially in the unbroken southern half of the larger ( $\sim 3$  kpc in diameter) and more energetic eastern supershell (see Figure 3 in Rand & van der Hulst 1993). The 1.5 GHz emission shown in the bottom panel is predominantly non-thermal emission, except in two specific star-forming regions, one of which coincides with this larger H I supershell (Irwin et al. 2012). Interestingly, the dust temperatures are lower and the X-ray emission is weaker outside of the expanding shock from the H I supershells. This X-ray “gap” between the expanding shell and the superbubble region is more noticeable around the larger shell.

Before we end this section, we wish to better quantify the size and morphology of the superbubble region. For this, we generated a radial profile of the  $S_{70}/S_{160}$  ratio perpendicular to the mid-plane passing through the galaxy center (slice width of one pixel,  $2.85''$ ). Figure 7 shows that the highest ratios,  $S_{70}/S_{160} \sim 0.9$ , are reached within the disk of the galaxy about  $\sim 10''$  from the disk mid-plane. A value of  $S_{70}/S_{160} \sim 0.5$  is a good lower limit ( $-1\sigma$ ) for the typical distribution of values observed in starburst galaxies (Meléndez et al. 2014). In the rest of the paper, we define the superbubble as the region where  $S_{70}/S_{160} \geq 0.5$ , excluding any FIR emission from within one scale height of the galaxy stellar continuum observed at  $4.5 \mu\text{m}$  (see McCormick et al. 2013, for details). The superbubble region defined in this way is shown in Figure 8. This figure emphasizes the fact that the superbubble is not symmetrically located with respect to the nucleus of NGC 4631, extending nearly  $\sim 5$  kpc north and west from the galaxy center.

## 4.2. SPIRE Colors

Figure 9 shows a comparison between the  $S_{250}/S_{350}$  and  $S_{250}/S_{500}$  ratios map and the neutral hydrogen gas. The superbubble is barely visible in the  $S_{250}/S_{350}$  ratio map (left panels). On the other hand, we see a good correspondence between the cold dust component and the large-scale H I spurs. This corroborates the results from our previous morphological comparisons of the SPIRE images and H I 21-cm maps and the cold dust distribution observed at 1.2 mm (Neininger & Dumke 1999). However, the SPIRE color map makes the connection between the cold extraplanar dust and the H I emission from Spurs 1, 2 and 4 more obvious, emphasizing a disk origin for these features. Again, Spur 3 appears to be disconnected from the galaxy disk, in agreement with previous results (Rand 1994).

The superbubble is more evident in the  $S_{250}/S_{500}$  ratio map (right panels in Figure 9), where slightly higher  $S_{250}/S_{500}$  values are observed in the northern region above the disk, suggesting a change in the spectral slope between 250 and  $500 \mu\text{m}$ . We will return to this result in Section 4.5 using a more quantitative analysis. There is also an excellent spatial correspondence between the larger H I supershell (east of the central region) and flatter spectral indices in Figure 9, suggesting

that the expanding H I shell is affecting the associated cold dust component by increasing its temperature (see discussion in Section 4.6). For these comparisons, we convolved the SPIRE images at 250 and 350  $\mu\text{m}$  to the SPIRE kernel at 500  $\mu\text{m}$  with a common pixel size of  $18.''4$  pixel $^{-1}$  (FWHM/2 of the SPIRE PSF at 500  $\mu\text{m}$ ) and then applied an adaptive median smoothing with a S/N = 10 per pixel with a direct local noise estimate.

### 4.3. Dust Masses

We determined the dust masses in NGC 4631 by fitting a single-temperature modified black-body (MBB) to the PACS and SPIRE data. For this, we used

$$F_\nu = \frac{M_d \kappa_\nu B_\nu(T_d)}{D^2}, \quad (1)$$

where  $M_d$  is the dust mass,  $B_\nu$  is the Planck function,  $T_d$  is the dust temperature,  $D$  is the distance to the galaxy, and  $\kappa_\nu$  is the dust emissivity,  $\kappa_\nu = \kappa_o(\nu/\nu_o)^\beta$ , where  $\kappa_o$  is the dust opacity at 350  $\mu\text{m}$ ,  $0.192 \text{ m}^2 \text{ kg}^{-1}$  (Draine 2003, hereafter, D03). This value of the dust opacity is based on the best fit of the average far-infrared dust emissivity for the Milky Way model presented in D03, which yields a best-fit spectral index value of  $\beta = 2.0$ . Caution must be taken as the normalized dust model opacity cross-section,  $\kappa_o$ , is associated with a dust model with  $\beta = 2.0$  and thus, discrepancies may arise between the results from a single-temperature MBB fit with a fixed emissivity and with an emissivity as a free parameter (see Bianchi 2013, for a review). In Figure 10, we present the best fit to the *Herschel* observations of the global emission from the galaxy with  $\beta = 2.0$  and the dust mass and temperature as free parameters. At wavelengths longer than  $\sim 20 \mu\text{m}$ , the infrared continuum is dominated by thermal radiation from dust grains. Time-dependent radiation from small dust grains (grains with radii,  $a \leq 50 \text{ \AA}$ ) dominates the continuum at wavelengths shorter than  $\sim 60 \mu\text{m}$  while, at longer wavelengths, the FIR continuum is dominated by larger size dust grains emitting at a more steady temperature (e.g., Draine 2003; Kennicutt & Evans 2012). Given the uncertainty on an “average temperature” for the small grain population and to avoid contamination to the larger dust grain emission, we use the 70  $\mu\text{m}$  flux as an upper limit in our fits.

The best single-temperature MBB fit with  $\beta = 2$  (fixed) gives a global dust mass of  $\log(M_d/M_\odot) = 7.61^{+0.04}_{-0.05}$  and  $T_d = 22.26 \pm 0.55 \text{ K}$  with  $\chi_r^2 = 0.59$ . If  $\beta$  is a free parameter then we obtain a dust mass of  $\log(M_d/M_\odot) = 7.51^{+0.05}_{-0.06}$ ,  $\beta = 1.65 \pm 0.18$ , and  $T_d = 24.98 \pm 44 \text{ K}$  with  $\chi_r^2 = 0.32$ . This latter fit thus results in a slightly hotter and lower dust mass than the single-temperature MBB fit with fixed  $\beta$ . In order to estimate the uncertainties in the fitted parameters we generated 200 SED created by randomly choosing a photometric data point within the observed errorbars. A best fit model is found for each SED and the uncertainties are taken as the  $1-\sigma$  distribution of the values for each parameter.

We also estimated the physical parameters associated with the dust in the disk and superbubble using the regions shown in Figure 8 (see Section 4.1). For the disk, the best single-temperature

MBB fit with a fixed  $\beta$  gives a dust mass of  $\log(M_d/M_\odot) = 7.56^{+0.04}_{-0.05}$  and  $T_d = 22.17 \pm 0.53$  K with  $\chi_r^2 = 0.63$ . Allowing  $\beta$  to vary as a free parameter we obtained a disk mass of  $\log(M_d/M_\odot) = 7.44^{+0.04}_{-0.05}$  and  $T_d = 25.17 \pm 1.45$  K with  $\chi_r^2 = 0.28$ . These values imply that the disk mass represents  $\sim 85 - 89\%$  of the total dust mass of the galaxy. A single-temperature MBB fit to the PACS and SPIRE values in the superbubble region gives:  $\log(M_d/M_\odot) = 6.16^{+0.05}_{-0.05}$  and  $T_d = 24.46 \pm 0.7$  K for  $\beta = 2.0$  (fixed) and, for  $\beta$  as a free parameter,  $\log(M_d/M_\odot) = 6.11^{+0.08}_{-0.10}$ ,  $\beta = 1.85 \pm 0.23$  and  $T_d = 25.82 \pm 2.21$  K (see Table 2). Thus, the dust mass of the superbubble represents  $\sim 4\%$  of the total dust mass of the galaxy. Figure 10 shows a comparison between the best-fit models for the global, disk and the superbubble observations. See Tables 1 and 2 for details on the fluxes in each region and the resulting fit parameters.

Our values for the dust masses in NGC 4631 can be compared with those in the literature (adjusted to our adopted distance of 7.4 Mpc). By fitting a single-temperature MBB to the observed global 70 – 450  $\mu\text{m}$  fluxes with an emissivity law with  $\beta = 2$ , Bendo et al. (2006) estimated the total dust mass for this galaxy to be  $\log(M_d/M_\odot) = 7.52$ , in good agreement with our results. Using a similar approach, Skibba et al. (2011) performed a fit to the 70 – 500  $\mu\text{m}$  fluxes densities in NGC 4631 and found a dust mass of  $\log(M_d/M_\odot) = 7.23 \pm 0.05$  and  $T_d = 27.7 \pm 0.8$  K. In their models they assumed a smaller spectral slope,  $\beta = 1.5$ , which yielded a higher temperatures than our two models ( $\beta = 2$  and  $\beta = 1.65 \pm 0.18$  derived from our best fit with  $\beta$  as a free parameter). The discrepancies in the temperature and dust mass may be explained by the different  $\beta$  and adopted dust opacity,  $\kappa_o(500\mu\text{m}) = 0.095 \text{ m}^2 \text{ kg}^{-1}$  (Bianchi 2013). Alternatively, the dust mass content in galaxies can be estimated by fitting the observed flux densities with a set of physical models of interstellar dust heated by a stellar radiation field (see Draine & Li 2007, for details). From this, Bendo et al. (2006) found a dust mass of  $\log(M_d/M_\odot) = 7.82$  by fitting the 1.0 - 1230  $\mu\text{m}$  fluxes of NGC 4631. This value agrees with the results from the best-fit models presented by Draine et al. (2007) with a dust mass  $\log(M_d/M_\odot) = 7.94$ , for a range of the maximum starlight intensity scale factor, and  $\log(M_d/M_\odot) = 7.78$ , for a fixed scale factor (see Bendo et al. 2006, for details). Overall, the dust masses derived from the best-fit physical models are a factor  $\sim 2$  higher than our estimates. As we mentioned before, the discrepancy between the two mass determinations has been studied in detail by Bianchi (2013) where it was found to be the result of a different (not consistent) absorption cross section between the two approaches. In our case, the absorption cross section normalization,  $\kappa_o$ , used in our MBB fit is taken from the grain model in D03 (with an implicit spectral slope of  $\beta = 2$ , see discussion above) whereas results from Draine et al. (2007) used a different grain size and composition.

The total gas mass in NGC 4631, adjusted for heavy elements, is  $\log(M_{\text{HI}+\text{H}_2}/M_\odot) = 10.05$  (Irwin et al. 2011), thus implying a gas-to-dust ratio of  $275^{+34}_{-24}$  if we use the dust mass derived from our best fit with a fixed  $\beta = 2.0$ . Using the best-fit dust mass with  $\beta$  as a free parameter, the gas-to-dust ratio is  $345^{+51}_{-38}$ . Overall, these values are a factor of  $\sim 2$  higher than the ratio for the Milky Way ( $\sim 140$ , see Table 2 in Draine et al. 2007). Our simple calculation does not include the contribution from the warmer dust component, which may bring the gas-to-dust ratio closer to the

Milky Way value, which is regarded as typical in spiral galaxies.

In an attempt to quantify the effect of the warm dust component, we attempted to fit the FIR fluxes of NGC 4631 as a combination of two MBB of different temperatures. However, given the number of free parameters (six in total) and the number of observed points, this two-temperature MBB fit is somewhat less constrained. For this reason, we also include in our analysis the fluxes at 450 and 850  $\mu\text{m}$  from the Submillimeter Common-User Bolometric Array (Dale et al. 2005), see Table 1. We perform the SED fit in the 70 – 850  $\mu\text{m}$  range with a fixed spectral index of  $\beta = 2$  for both components. The best-fit model is shown in Figure 11 (see Table 3 for details). We obtain a dust mass of  $\log(M_d/M_\odot) = 7.43^{+0.12}_{-0.16}$  and  $T_d = 24.45 \pm 3.75$  K in the warm component and a dust mass of  $\log(M_d/M_\odot) = 8.66^{+0.26}_{-0.60}$  and  $T_d = 6.68 \pm 3.81$  K in the colder component. Our results agree with those presented by Bendo et al. (2006) and their two thermal component approximation within our (large) uncertainties. The temperature of our cold dust component is higher, implying a gas-to-dust ratio for this component of  $25^{+73}_{-11}$ , which is closer to the Milky Way value within its uncertainty. Comparing our values for the warm and cold dust components, we find that our temperatures are lower than the values derived by Stevens et al. (2005) using a similar two-temperature greybody approximation with  $\beta = 2.0$  (38 K and 17 K for the warm and cold dust components, respectively). However, for this analysis, they used fluxes from *IRAS* (60 and 100  $\mu\text{m}$ ) that underpredict the observed global fluxes by a factor of  $\sim 1.5$  when compared with values from *Spitzer* and *Herschel*.

#### 4.4. Star Formation Rates

Finally, in order to estimate the SFR for this galaxy via the total infrared (IR; integrated over the 8 – 1000  $\mu\text{m}$  range) luminosity, we add a third component to fit the observed SED. Here, we also include in the fit the *Spitzer* observations at 5.8 and 8.0  $\mu\text{m}$  from IRAC and at 24  $\mu\text{m}$  from MIPS (Dale et al. 2009). Figure 11 shows the best-fit model with  $\log(M_d/M_\odot) = 8.66$  and  $T_d = 6.66$  K for the cold dust component,  $\log(M_d/M_\odot) = 7.43$  and  $T_d = 24.42$  K for the warm dust component, and  $\log(M_d/M_\odot) = 1.35$  and  $T_d = 221.8$  K for the hot dust component (see Table 3 for details). From a direct integration of the SED, the total 8 – 1000  $\mu\text{m}$  luminosity is  $\log(L_{\text{IR}}/L_\odot) = 10.30$ , which implies a SFR of  $3.47 M_\odot \text{ yr}^{-1}$  when using the SFR – IR calibration of Kennicutt (1998). Our value is slightly higher than those estimated from the total infrared luminosity based on the observed *IRAS* fluxes at 12, 25, 60, and 100  $\mu\text{m}$ ,  $\sim 2.9 M_\odot \text{ yr}^{-1}$  (corrected by our adopted distance to the source, Strickland et al. 2004; Tüllmann et al. 2006a). The SFR derived from a combination of the  $H\alpha$  and 24  $\mu\text{m}$  luminosities yields a value of  $1.6 M_\odot \text{ yr}^{-1}$  (corrected by our adopted distance to the source, Kennicutt et al. 2009; Calzetti et al. 2010). Note that dust extinction, especially in edge-on galaxies, can hamper the use of some of the star formation indicators that rely on short-wavelength emission such as  $H\alpha$ . Thus, we adopt our IR-based SFR value for the remainder of the paper. For comparison, in M82, the SFR derived from the total IR based on the *IRAS* fluxes is  $9.2 M_\odot \text{ yr}^{-1}$  (Strickland et al. 2004), largely in the nuclear starburst whereas in NGC 4631 the star

formation is widely distributed (e.g., Irwin et al. 2011).

#### 4.5. Pixel-by-Pixel SED fit

We also performed a pixel-by-pixel SED fit, where we only considered pixels with detection greater than  $3\sigma$  at all wavelengths. For this exercise, we converted the higher resolution PACS images to that of the SPIRE  $500\ \mu\text{m}$  PSF with a pixel size of  $18''\ \text{pixel}^{-1}$  (FWHM/2 of the SPIRE PSF at  $500\ \mu\text{m}$ ). Note that at  $18''$ , each pixel is not independent from its neighbors. However, a pixel size comparable to that of the  $500\ \mu\text{m}$  PSF ( $36''$ ) would have resulted in too few pixels to have a meaningful comparison. Therefore, results from our pixel-by-pixel approximation are intended for a quantitative analysis of the dust properties and distribution across the galaxy. Figure 12 shows the distribution of values for  $M_d$  and  $T_d$  by fitting all the observations with a single-temperature MBB and  $\beta = 2$ . Similarly, we performed a pixel-by-pixel SED fit with  $\beta$  as a free parameter, see Figure 13. As before, we performed the pixel-by-pixel SED fit assuming the observed flux at  $70\ \mu\text{m}$  is an upper limit to the actual flux at that wavelength. Figures 12-13 show that the dust mass is symmetrically distributed along the galaxy’s major axis. However, the temperature maps depend significantly on our assumption on fixing  $\beta$  or not.

The temperature map with  $\beta = 2$  follows roughly the morphology of the superbubble observed in the PACS  $S_{70}/S_{160}$  ratio map, with higher temperatures north of the nucleus, but it fails to show details in the active star formation regions across the galaxy disk. In contrast, the temperature map with floating spectral index shows more detail in the disk, with higher temperatures derived near the active star-forming regions in the disk observed in the PACS  $70\ \mu\text{m}$  and  $\text{H}\alpha$  images. In this case, however, it is the map of the spectral index,  $\beta$ , rather than the temperature map, that shows a closer spatial correspondence with the superbubble region (indicating  $\beta > 2$ ). Clearly, there is a degeneracy between  $T_d$  and  $\beta$  in these fits, so we cannot distinguish between the following two plausible scenarios: (1) the dusty material in the superbubble region is heated by star formation in the disk, the hot X-ray emitting material, or shocks, or (2) the dust in the superbubble region has a different (steeper) emissivity slope than that in the disk, perhaps indicating different intrinsic dust properties (e.g., grain size distribution and composition).

To further look into this issue, we produce pixel-by-pixel color-color diagrams to investigate the dust properties across the galaxy, see Figure 14. For this comparison, we adopt the superbubble region defined in Section 4.1. We also show the expected color-color relationship for a single-temperature MBB with two different emissivities,  $\beta = 2.0$  and  $1.5$ , and a range of temperatures ( $15\text{K} - 40\text{K}$ ). The dusty superbubble follows a color distribution that is different from that of the disk in the  $S_{250}/S_{500}$  versus  $S_{100}/S_{250}$  diagram (see Left panel in Figure 14), with higher  $S_{250}/S_{500}$  values, thus a steeper spectral slope, in the superbubble, suggesting a higher dust opacity. The right panel in Figure 14 shows the SPIRE colors,  $S_{250}/S_{350}$  versus  $S_{350}/S_{500}$ , where it can be seen that values from the superbubble have a steeper slope than those from the disk emission, therefore favoring scenario #2 over scenario #1.

#### 4.6. The Temperature and Spectral Index Relation

In our single-temperature MBB approximation, the fitted spectral index,  $\beta$ , carries important information about the dust opacity and composition. However, this simple approximation, used to describe the optically thin thermal emission from large grains radiating in thermal equilibrium, comes at a price: a degeneracy between  $\beta$  and temperature. Part of this degeneracy comes from the SED fitting (fitting technique, limited number of observations and flux uncertainties, e.g., Shetty et al. 2009a; Kelly et al. 2012), the single-temperature simplification employed to describe the dust temperature distribution along the line of sight (e.g., Shetty et al. 2009b), and real variations of the physical properties of the dust grain population (e.g., Meny et al. 2007; Coupeaud et al. 2011; Ysard et al. 2012). An anti-correlation between the dust temperature and the spectral index,  $\beta$ , has been observed in a number of sources based on a variety of experiments and observatories (e.g., Dupac et al. 2003; Désert et al. 2008; Paradis et al. 2010; Veneziani et al. 2010; Bracco et al. 2011; Smith et al. 2012; Davies et al. 2014; Hughes et al. 2014). For these reasons, one has to be cautious when interpreting the T- $\beta$  relation.

Our pixel-by-pixel analysis allows us to investigate the spatial distribution of the T- $\beta$  relation throughout the galaxy. Figure 15 shows the fitted temperatures as a function of the dust spectral index across the disk and the superbubble in NGC 4631. Our values show an inverse correlation between the dust temperature and spectral index with two different and well-separated relationships for the disk and the superbubble. This result is in excellent agreement with the resolved analysis of the dust and gas content in Andromeda (M31), where Smith et al. (2012) found that the T- $\beta$  relation measured within 3.1 kpc from the center of the galaxy is distinct from that derived further out (green solid and dot-dashed lines, Figure 15). The T- $\beta$  relation from Smith et al. (2012) for the outer region of M31 ( $3.1 < R < 15 \text{ kpc}$ ) is in good agreement with our values for the outer parts of the disk in NGC 4631 and with values derived from the global properties of the *Herschel* Virgo Cluster Survey (Davies et al. 2014), suggesting that the range of dust properties and conditions in NGC 4631 and M31 are similar to those found in the late-type galaxies that comprises the Virgo sample. On the other hand, the  $T - \beta$  relation for the inner region in M31 ( $R < 3.1 \text{ kpc}$ ) agree with our values for the superbubble in NGC 4631.

Interestingly, the radial break in the T- $\beta$  relation observed in NGC 4631 and M31 is not present in the edge-on spiral NGC 891 (Hughes et al. 2014). NGC 891 is almost perfectly edge-on ( $i > 89^\circ$ ), thus making radial variations harder to detect. Nevertheless, there are also no statistically significant variations of the spectral index along the vertical direction (Hughes et al. 2014). The best-fit relation for NGC 891 lies slightly below the distribution of points from the superbubble in NGC 4631 (dashed blue line in Figure 15). Submillimeter point sources from the ARCHEOPS catalog (Désert et al. 2008), mostly of Galactic origin, lie close to the T- $\beta$  relation of the outer disk region of NGC 4631, whereas the best-fit T- $\beta$  relation for the PRONAOS-based data on different regions of the Galactic ISM (Dupac et al. 2003) provides a good dividing line between the data points in the outer disk of NGC 4631 and those in the superbubble (see Figure 15).

The excellent agreement between the  $T$ - $\beta$  relations of NGC 4631 and M31 and their radial dependences suggests a similar physical origin. In both cases, the different relations between the inner and outer disk regions are likely an indication that the dust in these regions has physically distinct properties. This result is consistent with the different color distributions observed between the superbubble and the disk of NGC 4631 (Figure 14) and the observed spatial variations of the spectral index between 250 and 500  $\mu\text{m}$  (Figure 9). We return to this issue in the next section.

## 5. Discussion

The origin of the FIR emission in galaxies is unambiguously associated with thermal emission from heated dust grains. However, the identification of the heat source for the dust component requires further considerations. In galaxies without AGN, like NGC 4631, the amount of thermal emission from dust grains is often related to the ultraviolet continuum emission provided by young, massive stars. The good agreement between the morphology of the ionized gas ( $\text{H}\alpha$ ) and the warm-to-cold dust component in the disk of NGC 4631 is consistent with this picture. The origin and heat source of the extraplanar dust in NGC 4631 is less clear, however. The filamentary, chimney-like, and superbubble structures seen above the disk in the FIR, warm and hot ionized gas, and relativistic plasma suggest that some of the dust in the disk has been lifted out into the halo (e.g., Cooper et al. 2008). However, one must ask if stellar activity in the disk is energetically capable of lifting this material up to its observed position. In order to estimate the potential energy involved in lifting this material up to height  $z$  above the mid-plane of the galaxy, we assume an isothermal sheet model for the vertical distribution of light and mass in galactic disks (van der Kruit 1988), as presented by Howk & Savage (1997) for the dusty clouds in NGC 891 and later, by Rand (2000) for the molecular clouds in NGC 4631:

$$\Omega = 10^{52} \text{ ergs} \left( \frac{M}{10^5 M_\odot} \right) \left( \frac{z_o}{700 \text{ pc}} \right) \left( \frac{\rho_o}{0.185 \text{ M}_\odot \text{ pc}^{-3}} \right) \ln \left[ \cosh \left( \frac{z}{z_o} \right) \right], \quad (2)$$

where  $\rho_o$  is the mass density at the mid-plane,  $M$  is the mass of lifted material, and  $z_o$  is the mass scale height of the stellar disk. Here we use a mass scale height for the stellar disk of 1.5 kpc, as measured from the stellar disk observed at 4.5  $\mu\text{m}$  (McCormick et al. 2013). This value is in excellent agreement with the fit of the vertical distribution of the resolved stellar population for NGC 4631 observed with the *Hubble Space Telescope Advanced Camera for Surveys* (up to  $z_o = 1.4$  kpc, Seth et al. 2005b). Assuming an average mid-height for the superbubble region above the plane of about 3 kpc, and a conservative starting point at  $z = z_o$ , then the gain in potential energy is:

$$\Delta\Omega = 4 \times 10^{53} \text{ ergs} \left( \frac{\rho_o}{0.185 \text{ M}_\odot \text{ pc}^{-3}} \right). \quad (3)$$

Note that the main uncertainty on the prediction of the potential energy comes from the mass density at mid-plane, where we adopted a value of  $0.185 \text{ M}_\odot \text{ pc}^{-3}$ , representative of the total mass density at the solar position (see Bahcall 1984, for details). The potential energy required to lift the dust in the superbubble is thus comparable to that found by Irwin et al. (2011) for the CO ( $J = 3-2$ ) molecular clouds observed in the central region of NGC 4631, and an order of magnitude smaller than predictions from the CO ( $J = 1-0$ ) molecular clouds presented by Rand (2000). Note that we have conservatively assumed that the material come from  $z = z_0$  kpc. If the material starts at a distance ten times closer to the mid-plane,  $z_0 = 150$  kpc, then the energy needed to lift the material would be  $\sim 1.5$  times higher (note that eqn 2 is undefined at the mid-plane).

Assuming that dust and gas are mixed inside the superbubble with typical Galactic ratios (140, Draine et al. 2007), then the required energy to lift the material (gas and dust) into the halo is two orders of magnitude higher,  $\sim 6 \times 10^{55}$  ergs. Taken at face value, this energy is equivalent to the kinetic energy of  $\sim 60,000$  type II supernovae. Given the current SFR of NGC 4631 ( $\sim 3.5 \text{ M}_\odot \text{ yr}^{-1}$ , Section 4.4), and assuming SFR  $\sim 50$ -100 SNR, where SNR is the supernova rate, then this is equivalent to the kinetic energy injected by all supernovae produced in NGC 4631 in the past  $\sim 10^6$  yrs. This last number should be increased to take into account the fact that the superbubble structure is seen only in the inner  $\sim 6$  kpc, whereas star formation activity in NGC 4631 is distributed throughout the disk. The current level of star formation activity thus seems insufficient to lift the dust and gas out of the disk unless 100% of the kinetic energy from supernovae produced in the past  $\sim 10^6$  is tapped to lift this material above the disk. This scenario seems unlikely. The tension is reduced if the dust-to-gas ratio inside the superbubble is higher than the Galactic value. If the dust-to-gas ratio is Galactic, then one has to invoke that (1) the star formation rate was (much) higher in the past (e.g., Irwin et al. 2011) or (2) some of the dust inside the superbubble comes from material tidally stripped from nearby companions or disk material lifted during past interactions, a scenario that has also been evoked to explain the large-scale dusty halo of M82 (Roussel et al. 2010).

Our data do not allow us to distinguish between these two scenarios. The presence of two highly energetic supershells in the disk with kinetic energies of  $2 - 5 \times 10^{54}$  ergs (Shell 1 on the east side, expanding at  $45 \text{ km s}^{-1}$ ) and  $0.6 - 1 \times 10^{54}$  ergs (Shell 2 on the west side, expanding at  $35 \text{ km s}^{-1}$ ) is difficult to reconcile with the current level of star formation (Rand & van der Hulst 1993; Wang et al. 1995) and thus favors scenario (1) (unless these shells are produced instead in an oblique impact of a high velocity cloud with the galactic disk (Rand & Stone 1996)). These supershells are no doubt releasing large amounts of energy into the surrounding ISM via shocks from the shells expanding into the surrounding ISM, changing the shape of the dusty halo, and perhaps even causing the asymmetric geometry of the superbubble (Section 4.1).

On the other hand, there is also considerable evidence that past galaxy interactions are at least partly responsible for the existence and peculiar morphology of the giant gaseous halo of NGC 4631 (e.g., Hummel et al. 1988; Hummel & Dettmar 1990; Rand 2000; Wang et al. 2001). Numerical simulations for the H I tidal streams in the three-galaxy system NGC 4631, NGC 4656,



and NGC 4627 have suggested that NGC 4627 has been a source of cold gas in the past Combes (1978). This dwarf elliptical galaxy is the closest companion to NGC 4631 and is undetected in our *Herschel* images and thus dust depleted. This picture is also supported by the morphology of the superbubble which extends towards NGC 4627. In particular, there is a stream of warm dust that extends directly below NGC 4627 at the southwest end of the FIR, radio, and soft X-ray loop, as discussed in Section 3.

Regardless of the exact origin of the dust in the halo of NGC 4631, the FIR ratio maps presented in Section 4 indicate that dust in the superbubble region has a different (steeper) emissivity spectral slope than dust in the disk. Dust in the superbubble may be heated by UV radiation from the on-going star formation activity in the disk, X-ray bremsstrahlung radiation from the extraplanar hot plasma at the position of the superbubble, or by shocks from a large-scale star-formation driven wind (e.g., Strickland et al. 2004). All of these processes may alter the intrinsic dust properties inside the superbubble by destroying the more fragile grains, e.g., via thermal sputtering and grain shattering (grain-grain collision). These mechanisms often favor the destruction of the smaller grains (e.g., sputtering, Jurac et al. 1998; Raymond et al. 2013), and thus may change the overall dust grain size distribution in favor of larger grains. This may help explain the different SPIRE colors and T- $\beta$  relations observed in the disk and superbubble region.

## 6. Conclusions

We present the results from a detailed analysis of deep *Herschel* PACS and SPIRE images in the nearby edge-on star-forming galaxy NGC 4631. Given the superior angular resolution and sensitivity of *Herschel*, we were able to carry out a spatially resolved analysis of the dust distribution in this object. We complement our analysis of these data with published observations at other wavelengths to build a more complete picture of the multi-phase ISM in this galaxy. The main results can be summarized as follows:

- The PACS images at  $70\ \mu\text{m}$  (PSF FWHM  $\sim 5.6''$ ) and  $160\ \mu\text{m}$  (PSF FWHM  $\sim 11.4''$ ) show a rich complex of filaments and chimney-like features that extend up to  $\sim 6$  kpc above the galaxy disk. Many of the structures seen in the FIR coincide spatially with those seen in  $\text{H}\alpha$ , radio-continuum, and soft X-ray emission. This spatial match suggests a tight disk-halo connection regulated by star formation.
- The extraplanar emission detected on larger scale in the SPIRE images shows a good match with many of the extraplanar H I 21-cm spurs of NGC 4631. Most of these features likely are left-over tidal debris from recent interactions between NGC 4631 and its galaxy companions.
- A bubble-like structure that extends up to  $\sim 6.0$  kpc above the plane of the galaxy is detected in the PACS  $70/160\ \mu\text{m}$  ratio map. A pixel-by-pixel fit of the spectral energy distribution indicates that the dust in this region has a higher temperature and/or an emissivity with a

steeper spectral index than the dust in the disk. The superbubble region also shows higher  $S_{250}/S_{500}$  and  $S_{350}/S_{500}$  flux ratios than those observed in the disk, consistent with a steeper spectral index in this region. Dust inside the superbubble is heated by UV radiation from young stars in the disk, X-ray emission from the hot plasma in the halo, or shocks associated with a large-scale outflow into the halo. All of these processes may alter the dust grain size distribution inside the superbubble, and explain the higher spectral index of the dust emissivity in this region.

- The dust mass of the superbubble represents about  $\sim 4\%$  of the total dust mass in this galaxy. The energy required to lift this dusty material in the superbubble region is at least  $\sim 6 \times 10^{55}$  ergs, assuming a Galactic dust-to-gas ratio. The current rate of energy injection into the ISM by star formation activity in the disk appears to be energetically insufficient to lift this material into the halo, unless the dust-to-gas ratio is significantly higher than the Galactic value. One possible explanation is that the star formation rate was significantly higher in the past. The presence of two highly energetic H I supershells in the disk of this galaxy is consistent with this scenario and may still be shaping the gaseous halo. Another possibility is that some of the dust observed in the halo was deposited there from past galaxy interactions, either lifted directly from the disk of NGC 4631 or stripped from now dust-depleted companions (e.g., dwarf elliptical NGC 4627). In this regard, NGC 4631 could be a twin of M82 where tidal interactions seem to be more efficient at depositing dust into the halo than the star-formation driven wind (Roussel et al. 2010).

We are very grateful to Hélène Roussel for her help with the use of *Scanamorphos*. We also thank Richard Rand and Judith Irwin for generously making their published data available to us. Support for this work was provided by NASA through Herschel contracts 1427277 and 1454738 (S.V. and M.M.). This work has made use of NASAs Astrophysics Data System Abstract Service and the NASA/IPAC Extragalactic Database (NED), which is operated by the Jet Propulsion Laboratory, California Institute of Technology, under contract with the National Aeronautics and Space Administration. PACS has been developed by a consortium of institutes led by MPE (Germany) and including UVIE (Austria); KU Leuven, CSL, IMEC (Belgium); CEA, LAM (France); MPIA (Germany); INAF-IFSI/OAA/OAP/OAT, LENS, SISSA (Italy); IAC (Spain). This development has been supported by the funding agencies BMVIT (Austria), ESA-PRODEX (Belgium), CEA/CNES (France), DLR (Germany), ASI/INAF (Italy), and CICYT/MCYT (Spain). SPIRE has been developed by a consortium of institutes led by Cardiff University (UK) and including Univ. Lethbridge (Canada); NAOC (China); CEA, LAM (France); IFSI, Univ. Padua (Italy); IAC (Spain); Stockholm Observatory (Sweden); Imperial College London, RAL, UCL-MSSL, UKATC, Univ. Sussex (UK); and Caltech, JPL, NHSC, Univ. Colorado (USA). This development has been supported by national funding agencies: CSA (Canada); NAOC (China); CEA, CNES, CNRS (France); ASI (Italy); MCINN (Spain); SNSB (Sweden); STFC, UKSA (UK); and NASA (USA). HIPE is a joint development (are joint developments) by the Herschel Science Ground Segment Consortium, consisting of ESA, the NASA Herschel Science Center, and the HIFI, PACS and SPIRE consortia.

### A. Nature of the Brightest X-ray sources in NGC 4631

Many bright X-ray point sources have been detected in the disk of NGC 4631 (e.g., Vogler & Pietsch 1996; Wang et al. 1995; Read et al. 1997; Winter et al. 2006, 2007; Soria & Ghosh 2009). These X-ray sources represent possible candidates for blowing out gas and dust from the disk into the halo, and heating the dust. Figure 16 shows some of the X-ray sources overlaid on top of the PACS  $S_{70}/S_{160}$  ratio map. South of the dusty loop at the edge of the superbubble (at  $\alpha$  12<sup>h</sup>42<sup>m</sup>04<sup>s</sup>.2,  $\delta$  +32°28′50″, J2000.0 and  $\sim 4$  kpc from the nucleus), there is a X-ray source, source #5. This source was identified by Vogler & Pietsch (1996) (H10) in the X-ray (0.1 - 2.4 keV) as a very bright source tentatively located in the spiral arm of NGC 4631. The location outside the halo is consistent with the difference in X-ray spectral index of the source relative to that of the surrounding diffuse emission (Read et al. 1997). This source is thus unlikely to provide any contribution to the FIR bright halo.

Interestingly, two of the X-ray point sources, namely source #1 (Read et al. 1997) and source #7 (H7 in Vogler & Pietsch 1996), approximately coincide with the centers of the two large supershells observed in H I (Rand & van der Hulst 1993). It is clear from the PACS  $S_{70}/S_{160}$  ratios that the regions enclosed in the supershells show higher dust temperatures (ratios), suggesting that the supershells may be filled with warm dust despite being depleted of cold gas (to the extent of the sensitivity of H I observations). Source #7 is at the center of the smaller H I supershell (1.8 kpc in diameter, Shell 2) and is a fairly typical power-law ultra luminous X-ray source (ULX), perhaps powered by accretion onto a black hole (BH) with a mass  $\leq 50M_{\odot}$  (Soria & Ghosh 2009). The source has been observed several times and it shows little evidence for X-ray variability within the *Chandra* and *XMM-Newton* exposures with an intrinsic X-ray luminosity in the 0.3-10.0 keV band of  $(3.8 \pm 0.1) \times 10^{39}$  ergs s<sup>-1</sup> and  $(5.0 \pm 0.2) \times 10^{39}$  ergs s<sup>-1</sup> as estimated from *Chandra* and *XMM-Newton* observations, respectively (Soria & Ghosh 2009). In another study, Winter et al. (2006) estimated a BH mass of  $5.5 M_{\odot}$  for this source and an accretion rate  $L/L_{Edd}$  of 0.84, consistent with a normal stellar black hole X-ray binary. As we mentioned in Section 5, the required input energy to produce the kinematics of the H I shell 2 is about  $0.6 - 1.0 \times 10^{54}$  erg s<sup>-1</sup> and cannot be uniquely explained by the cumulative action of stellar winds and supernova explosions.

On the other hand, the larger supershell (Shell 1) surrounds a prominent star formation complex approximately at the same position as X-ray source #1 (Read et al. 1997). This region is dominated by the radio thermal emission with a 1.5 GHz spectral index of  $\alpha = -0.16 \pm 0.009$  (Irwin et al. 2012). It also shows an extended FIR morphology characterized by high dust temperatures indicative of UV heating from stellar activity. Of all the X-ray sources in the disk, this source is the weakest, with an X-ray luminosity in the 0.1-2.0 keV band of  $3 \times 10^{38}$  ergs s<sup>-1</sup> (Read et al. 1997). Because of this, the nature of this X-ray source is still unknown.

Another interesting X-ray source is #2, first detected as a luminous supersoft source by *ROSAT*/PSPC observations (Vogler & Pietsch 1996). Soria & Ghosh (2009) have suggested that this highly variable supersoft ULX could be the result of transient super-Eddington outbursts pow-

ered by non-steady nuclear burning on the surface of a massive white dwarf, perhaps as an extreme subclass of supersoft ULXs. However, the four-hour modulation observed in this source remains unexplained Carpano et al. (2007); Soria & Ghosh (2009). Adding to the interesting properties of this source is the fact that it is invisible in our PACS ratio map. This source is in the lower PACS ratio region between the larger H I surpershell and the superbubble region.

The other two sources, #3 and #4, are close to the center of the galaxy and appear as bright hot spots in our PACS ratio map, below the superbubble. The X-ray analysis of these sources suggest stellar black holes in different accretion states (e.g., Soria & Ghosh 2009).

Table 1. Flux Densities measured in NGC 4631

Instrument	$\lambda$ $\mu\text{m}$	Flux Jy
(1)	(2)	(3)
Global		
PACS	70	$141.9 \pm 14.2$
PACS	100	$232.9 \pm 23.3$
PACS	160	$247.0 \pm 24.7$
SPIRE	250	$111.4 \pm 11.1$
SPIRE	350	$50.0 \pm 5.0$
SPIRE	500	$19.9 \pm 2.0$
SCUBA <sup>a</sup>	450	$30.7 \pm 10.0$
SCUBA <sup>a</sup>	850	$5.7 \pm 1.2$
Disk		
PACS	70	$121.4 \pm 12.1$
PACS	100	$202.8 \pm 20.3$
PACS	160	$211.9 \pm 21.2$
SPIRE	250	$98.3 \pm 9.8$
SPIRE	350	$43.9 \pm 4.4$
SPIRE	500	$17.7 \pm 1.8$
Superbubble		
PACS	70	$8.2 \pm 0.8$
PACS	100	$15.4 \pm 1.54$
PACS	160	$11.7 \pm 1.2$
SPIRE	250	$5.8 \pm 0.6$
SPIRE	350	$2.2 \pm 0.2$
SPIRE	500	$0.8 \pm 0.1$

Note. — Column 1: Instrument. Column 2: Central wavelength of the observed band. Column 3: Flux density

<sup>a</sup>Flux densities measured with the Submillimeter Common-User Bolometric Array (SCUBA Dale et al. 2005)

Table 2. Parameters derived from Single-temperature Modified Blackbody Fits

Region	$\log M_d$ $M_\odot$	$T_d$ (K)	$\beta$	$\chi_r^2$
(1)	(2)	(3)	(4)	(5)
$\beta = 2.0$				
Total	$7.61^{+0.04}_{-0.05}$	$22.26 \pm 0.55$	...	0.59
Disk	$7.56^{+0.04}_{-0.05}$	$22.17 \pm 0.53$	...	0.63
Superbubble	$6.16^{+0.05}_{-0.05}$	$24.46 \pm 0.77$	...	0.51
$\beta$ Free				
Total	$7.51^{+0.05}_{-0.06}$	$24.98 \pm 1.44$	$1.65 \pm 0.18$	0.32
Disk	$7.44^{+0.05}_{-0.06}$	$25.17 \pm 1.45$	$1.62 \pm 0.16$	0.28
Superbubble	$6.11^{+0.08}_{-0.10}$	$25.82 \pm 2.21$	$1.85 \pm 0.23$	0.58

Note. — Column 1: Region where the fluxes are extracted. Column 2: Dust mass. Column 3: Dust temperature. Column 4: Spectral slope of the dust emissivity. Column 5: reduced chi-square of the fit.

Table 3. Global Parameters derived from Multiple Component Modified Blackbody Fits with  $\beta = 2.0$

Component	$\log M_d$ $M_\odot$	$T_d$ (K)	$\chi_r^2$
(1)	(2)	(3)	(4)
Two-temperature MBB			
Component 1	$7.43^{+0.12}_{-0.16}$	$24.45 \pm 3.75$	1.04
Component 2	$8.66^{+0.26}_{-0.60}$	$6.68 \pm 3.81$	...
Three-temperature MBB			
Component 1	$1.35^{+0.13}_{-0.17}$	$221.81 \pm 5.15$	3.17
Component 2	$7.43^{+0.13}_{-0.14}$	$24.42 \pm 3.75$	...
Component 3	$8.66^{+0.24}_{-0.61}$	$6.66 \pm 3.81$	...

Note. — Column 1: Dust component. Column 2: Dust mass. Column 3: Dust temperature. Column 4: reduced chi-square of the fit.



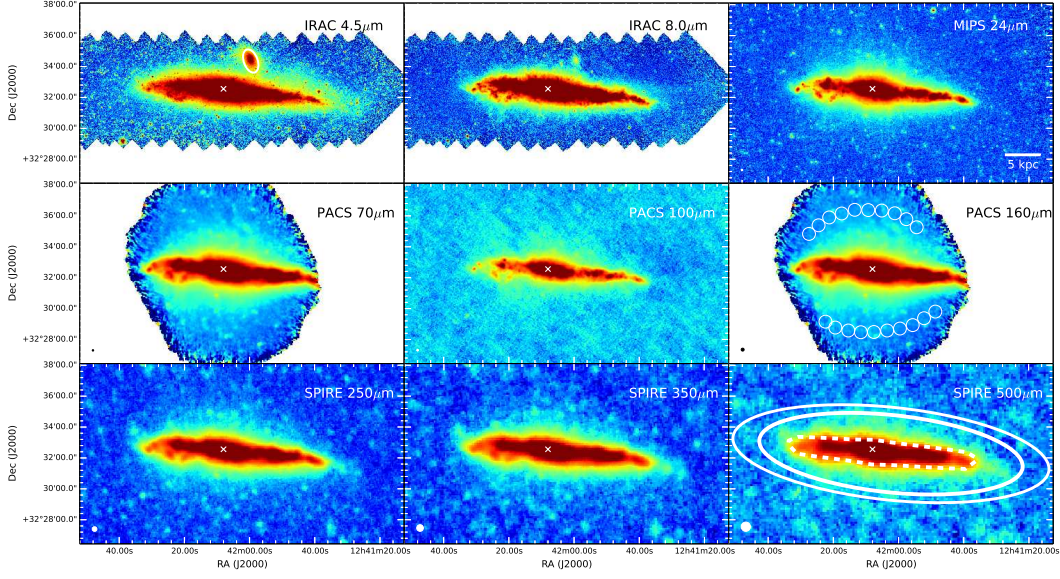


Fig. 1.— Comparison between Spitzer IRAC 4.5 and 8  $\mu\text{m}$  (McCormick et al. 2013), MIPS 24  $\mu\text{m}$  (Dale et al. 2009), PACS 70, 100, and 160  $\mu\text{m}$ , and SPIRE 250, 350, and 500  $\mu\text{m}$  for NGC 4631. The images are displayed with an inverse hyperbolic sine scaling. All the images are presented in their native resolution and pixel size:  $1.22'' \text{ pixel}^{-1}$  for the IRAC data, 1.4 and  $2.85'' \text{ pixel}^{-1}$  (FWHM/4) for the PACS data at 70 and 160  $\mu\text{m}$ , respectively, 4.5, 6.26, and  $9'' \text{ pixel}^{-1}$  (FWHM/4) for the SPIRE data at 250, 350, and 500  $\mu\text{m}$ , respectively. North is up and east is to the left in all of the images. The horizontal line in the lower right corner of the upper right panel represents 5 kpc. The panel of the 160  $\mu\text{m}$  emission shows the sky apertures used for the smaller field of view observations (OT1\_sveilleu\_2). The panel of the 500  $\mu\text{m}$  emission shows the photometric apertures used for the global flux and sky background (solid line) and the disk region within one vertical scale height of the galaxy mid-plane, derived from the IRAC 4.5  $\mu\text{m}$  image (dashed line, McCormick et al. 2013). For the sake of comparison throughout the paper, the solid white ellipse in the 4.5  $\mu\text{m}$  panel encompasses the companion galaxy NGC 4627. The beam size at each wavelength is indicated by a white/black filled circle in the bottom left corner of each panel. In all of the panels, the white “X” indicates the position of the infrared nucleus (Aaronson 1978, 1981).

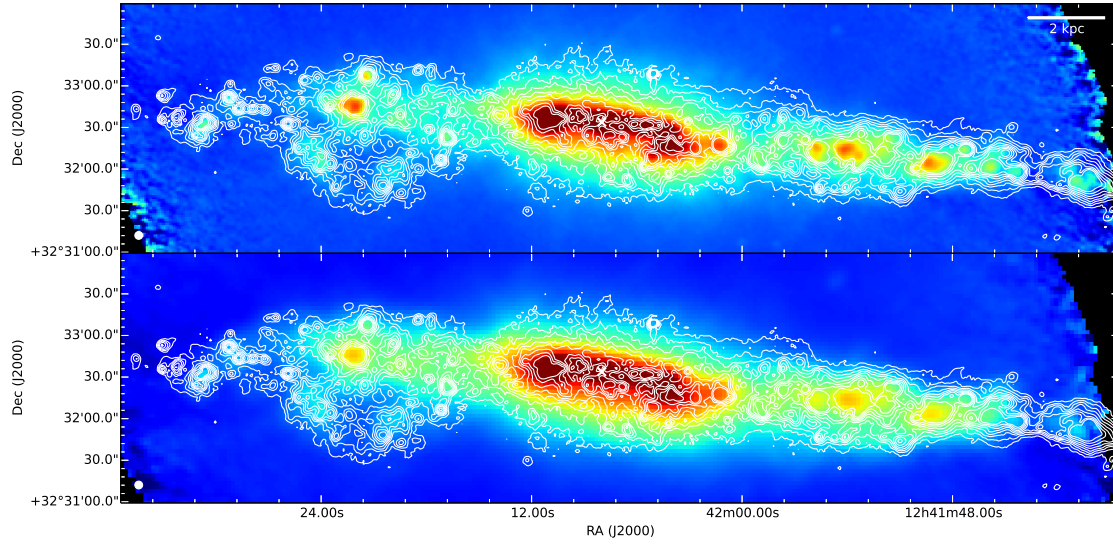


Fig. 2.—  $H\alpha$  emission from the warm ionized gas overlaid as contours on the PACS images at  $70\ \mu\text{m}$  (top panel) and  $160\ \mu\text{m}$  (bottom). The PACS maps are shown on a pixel scale of  $1.4$  and  $2.85''$   $\text{pixel}^{-1}$  at  $70$  and  $160\ \mu\text{m}$ , respectively. The contour levels are 20, 50, 100, 250, 1000, and 2000 times  $4 \times 10^{34}\ \text{ergs s}^{-1}$ . North is up and east is to the left in both panels. The horizontal line in the upper right corner of the upper panel represents 2 kpc. The beam size at each wavelength is indicated by a white filled circle in the bottom left corner of each panel. In all of the panels, the white “X” indicates the position of the infrared nucleus (Aaronson 1978, 1981).

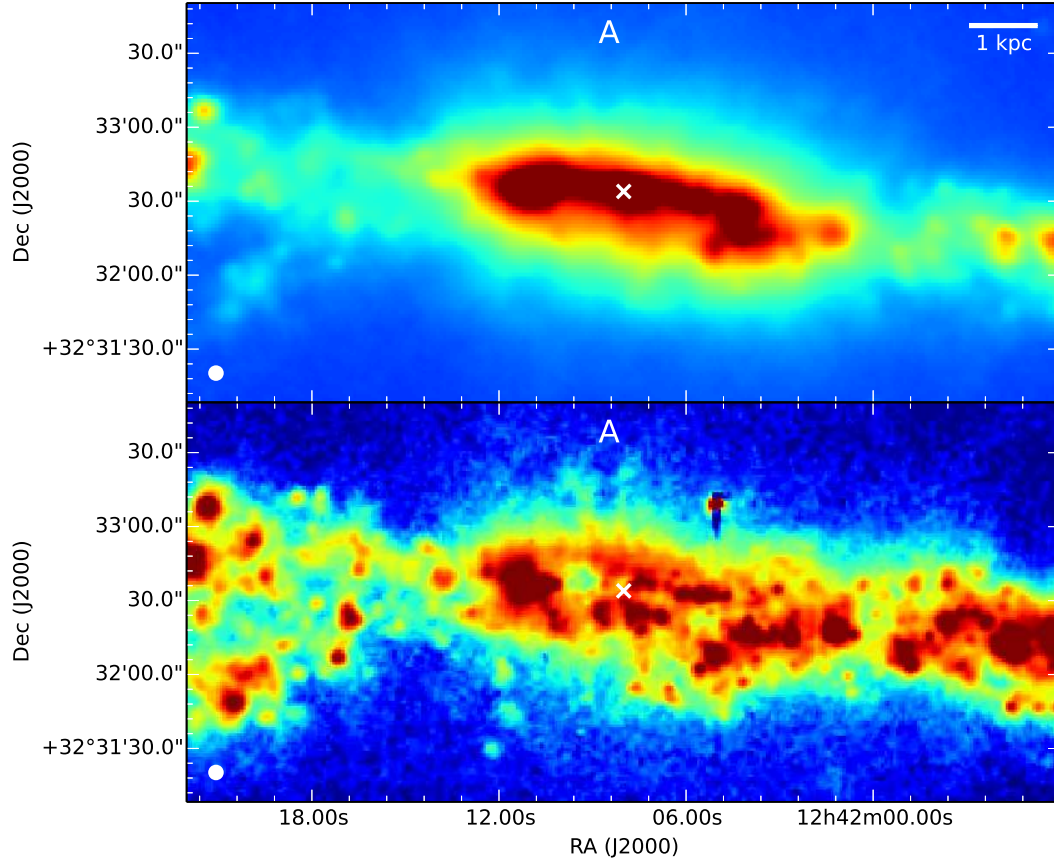


Fig. 3.— A close-up view of the central region of NGC 4631, comparing the PACS image at  $70\ \mu\text{m}$  (*upper-panel*) and the  $\text{H}\alpha$  map (*lower-panel*). The label “A” indicates the position of the  $\text{H}\alpha$  double-worm structure in both images. The PACS  $70\ \mu\text{m}$  map is presented on a pixel scale of  $1.4''\ \text{pixel}^{-1}$ , whereas the  $\text{H}\alpha$  map is shown on a pixel scale of  $1.2''\ \text{pixel}^{-1}$ . North is up and east is to the left in all of the images. The horizontal line in the upper right corner of the upper panel represents 1 kpc. The beam size at each wavelength is indicated by a white filled circle in the bottom left corner of each panel. In all of the panels, the white “X” indicates the position of the infrared nucleus (Aaronson 1978, 1981).

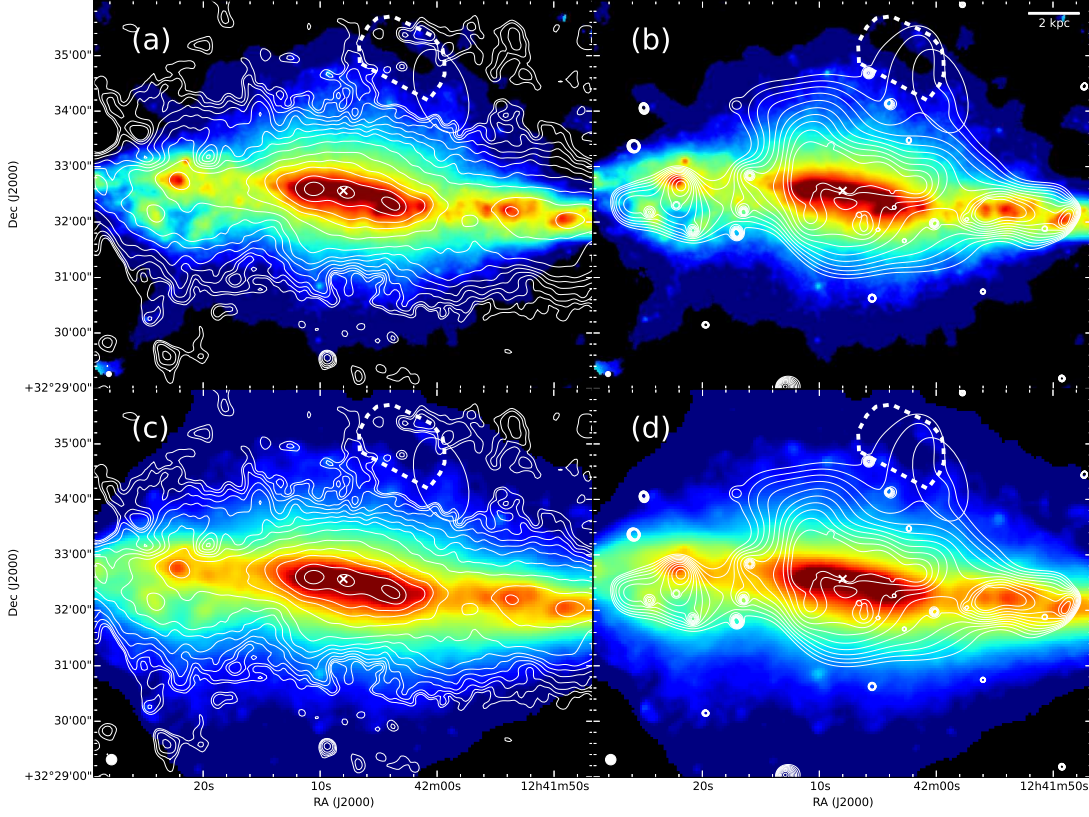


Fig. 4.— Adaptively smoothed PACS flux maps at 70 and 160  $\mu\text{m}$  compared with radio-continuum and soft X-ray images. (a) 70  $\mu\text{m}$  image with a pixel scale of  $1.4'' \text{ pixel}^{-1}$  is compared with the Robust 2 weighted image at 1.5 GHz, shown as contours. (b) 70  $\mu\text{m}$  smoothed map with a pixel scale of  $1.4'' \text{ pixel}^{-1}$  is compared with the *Chandra* soft X-ray (0.3 – 2.0 keV) emission, shown as contours. (c) and (d) Same as (a) and (b), but with the 160  $\mu\text{m}$  smoothed map on a pixel scale of  $2.85'' \text{ pixel}^{-1}$ . The contours for the 1.5 GHz image are at 9 ( $2\sigma$ ), 13.5, 20, 30, 45, 65, 90, 150, 300, 500, 750, 1500, and  $2500 \times 10\mu\text{Jy beam}^{-1}$ . The contours for the X-ray image are 0.1, 0.107, 0.114, 0.123, 0.135, 0.151, 0.172, 0.202, 0.243 and 0.301 photon  $\text{cm}^{-2} \text{ s}^{-1} \text{ arcsec}^{-2}$ . North is up and east to the left. The horizontal line in the upper right corner of panel (b) represents 2 kpc. The white ellipse indicates the position of the companion galaxy NGC 4627. The beam size at 70 and 160  $\mu\text{m}$  is indicated by a white filled circle in the bottom left corner of each panel. White dashed curves show the FIR loop discussed in Section 3. In all of the panels, the white “X” indicates the position of the infrared nucleus (Aaronson 1978, 1981).



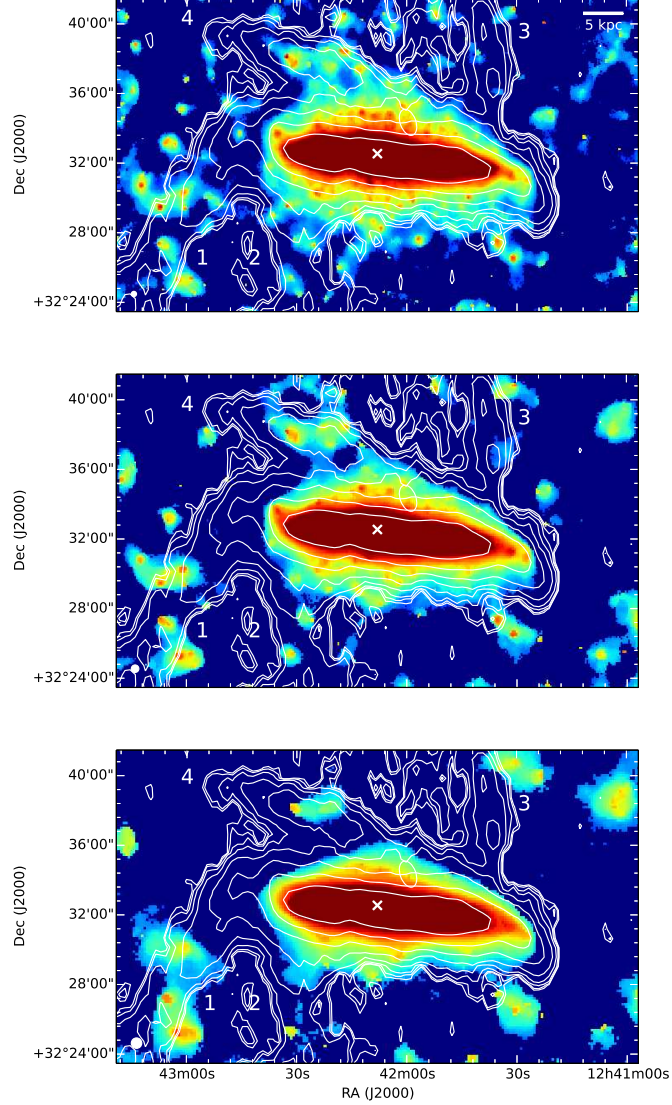


Fig. 5.— The H I 21-cm emission at  $45'' \times 87''$  resolution (shown as contours) overlaid on the adaptively smoothed SPIRE images at 250 (upper panel), 350 (middle panel), and 500 (lower panel)  $\mu\text{m}$  with a pixel scale of 4.5, 6.26, and  $9'' \text{ pixel}^{-1}$  (FWHM/4), respectively. In column density units at the beam center, the contour levels are 0.5, 0.6, 0.8, 1.3, 2.6, 5.7, 12.9, 30.1 and  $70.7 \times 10^{20} \text{ cm}^{-2}$ . Only fluxes above  $3 \sigma$  are shown in these panels. North is up and east is to the left in all of the images. The horizontal line in the upper right corner of the upper panel represents 5 kpc. The white ellipse indicates the position of the companion galaxy NGC 4627. The beam size at each wavelength is indicated by a white filled circle in the bottom left corner of each panel. In all of the panels, the white “X” indicates the position of the infrared nucleus (Aaronson 1978, 1981).

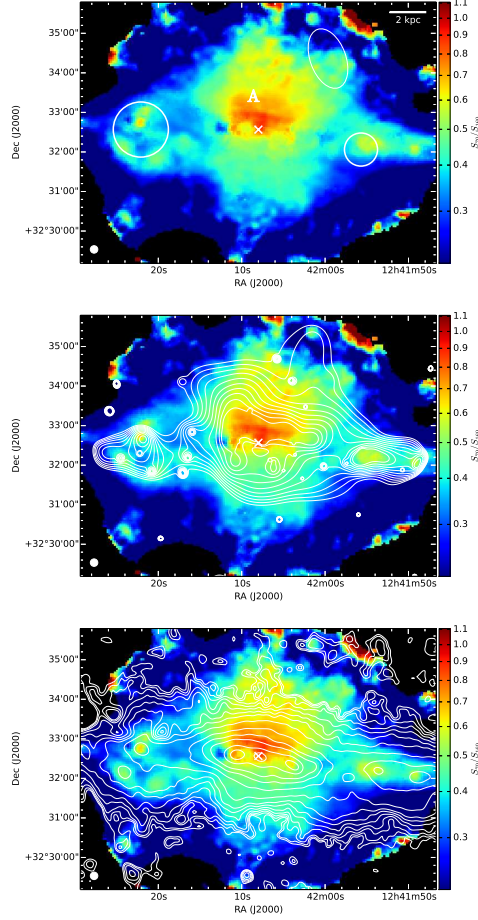


Fig. 6.— The  $S_{70}/S_{160}$  ratio map of the adaptively smoothed PACS maps shown in Figure 4. The upper panel shows the PACS ratio,  $S_{70}/S_{160}$ , with a pixel scale of  $2.85'' \text{ pixel}^{-1}$ . The middle panel shows the soft X-ray emission (Strickland et al. 2004), shown as contours, over the  $S_{70}/S_{160}$  ratio map. The contours are 0.1, 0.107, 0.114, 0.123, 0.135, 0.151, 0.172, 0.202, 0.243 and 0.301 photon  $\text{cm}^{-2} \text{ s}^{-1} \text{ arcsec}^{-2}$ . The lower panel shows the Robust 2 weighted 1.5 GHz image (Irwin et al. 2012), shown as contours, over the  $S_{70}/S_{160}$  ratio map. The contours are at 9 ( $2\sigma$ ), 13.5, 20, 30, 45, 65, 90, 150, 300, 500, 750, 1500, and  $2500 \times 10\mu\text{Jy beam}^{-1}$ . North is up and east is to the left. The horizontal line in the upper right corner of the upper panel represents 2 kpc. Note the X-ray and radio loop located  $\sim 6$  kpc north of the galaxy center. The white ellipse indicates the position of the companion galaxy NGC 4627. The white circles represent the approximate size of the H I supershells (Rand & van der Hulst 1993). The label “A” indicates the position of the H $\alpha$  double-worm structure (see Figure 3) and the white “X” indicates the position of the infrared nucleus (Aaronson 1978, 1981). The beam size at 160  $\mu\text{m}$  is indicated by a white filled circle in the bottom left corner of each panel.

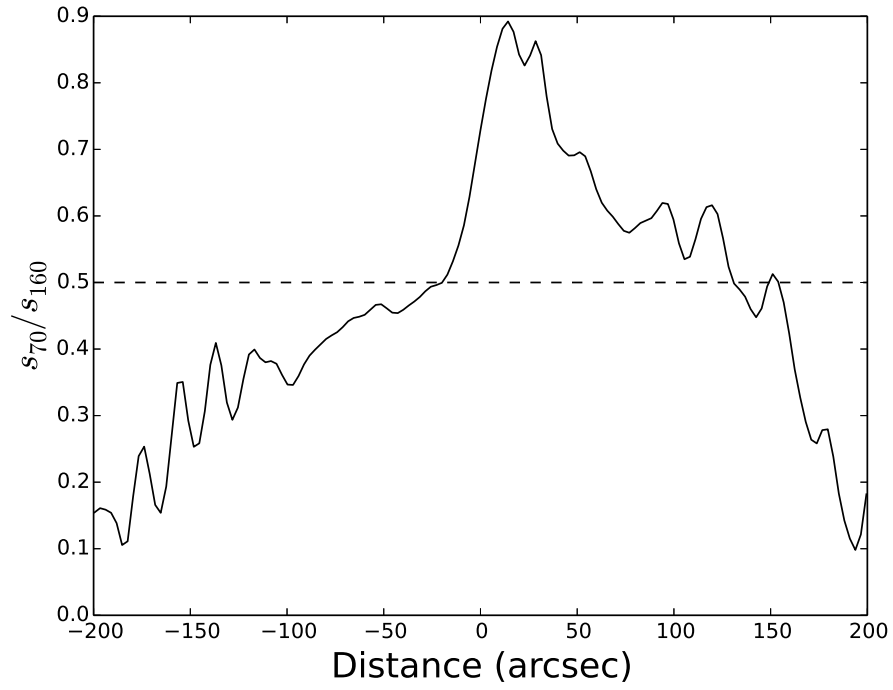


Fig. 7.— Vertical profile of the PACS  $S_{70}/S_{160}$  ratio with a slice width of one pixel,  $2.85''$ , perpendicular to the mid-plane passing through the galaxy center of NGC 4631. The origin of the horizontal axis corresponds to the disk mid-plane. The horizontal dotted line corresponds to  $S_{70}/S_{160} = 0.5$ . Values above this line mark the position of the superbubble region, shown in the next figure.

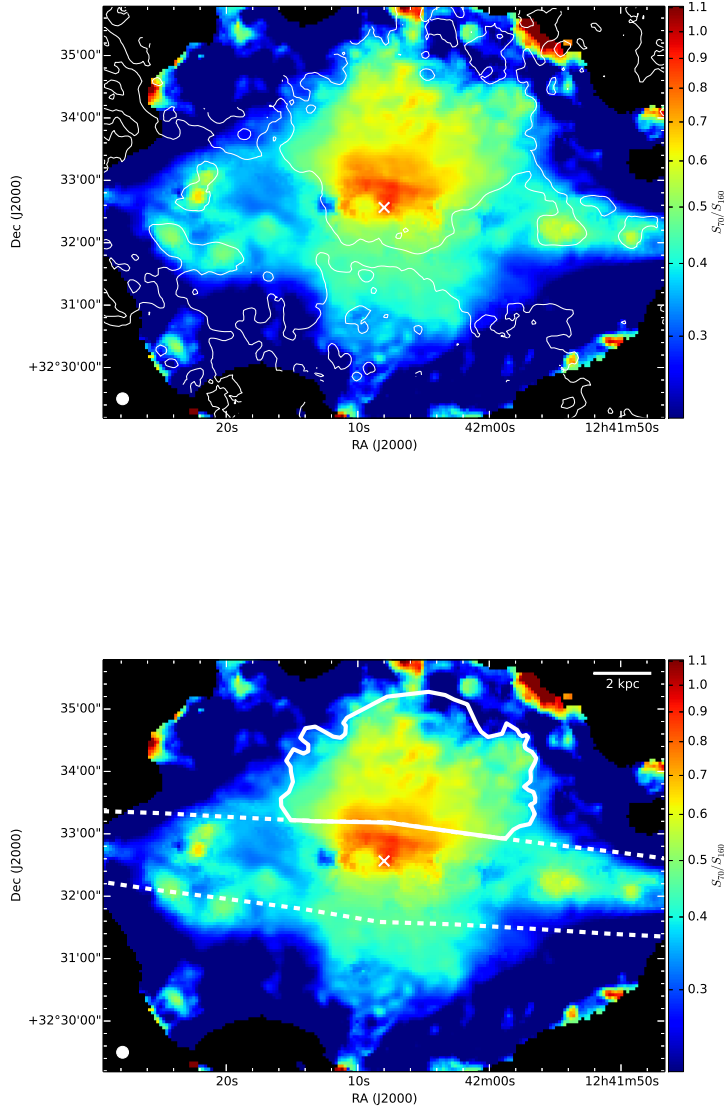


Fig. 8.— The  $S_{70}/S_{160}$  ratio map derived from the adaptively smoothed PACS maps shown in Figure 4. The pixel scale is  $2.85'' \text{ pixel}^{-1}$ . The contours in the upper panel represent a value of  $S_{70}/S_{160} = 0.5$ , used to define the superbubble region. The lower panel shows the region that is used to calculate the flux in the superbubble (solid line) and the disk region within one vertical scale height of the galaxy mid-plane, derived from IRAC 4.5  $\mu$ m image (dashed line, McCormick et al. 2013). North is up and east is to the left. The horizontal line in the upper right corner of the lower panel represents 2 kpc. The beam size at 160  $\mu$ m is indicated by a white filled circle in the lower left corner of the lower panel. A small “X” marks the position of the nucleus.



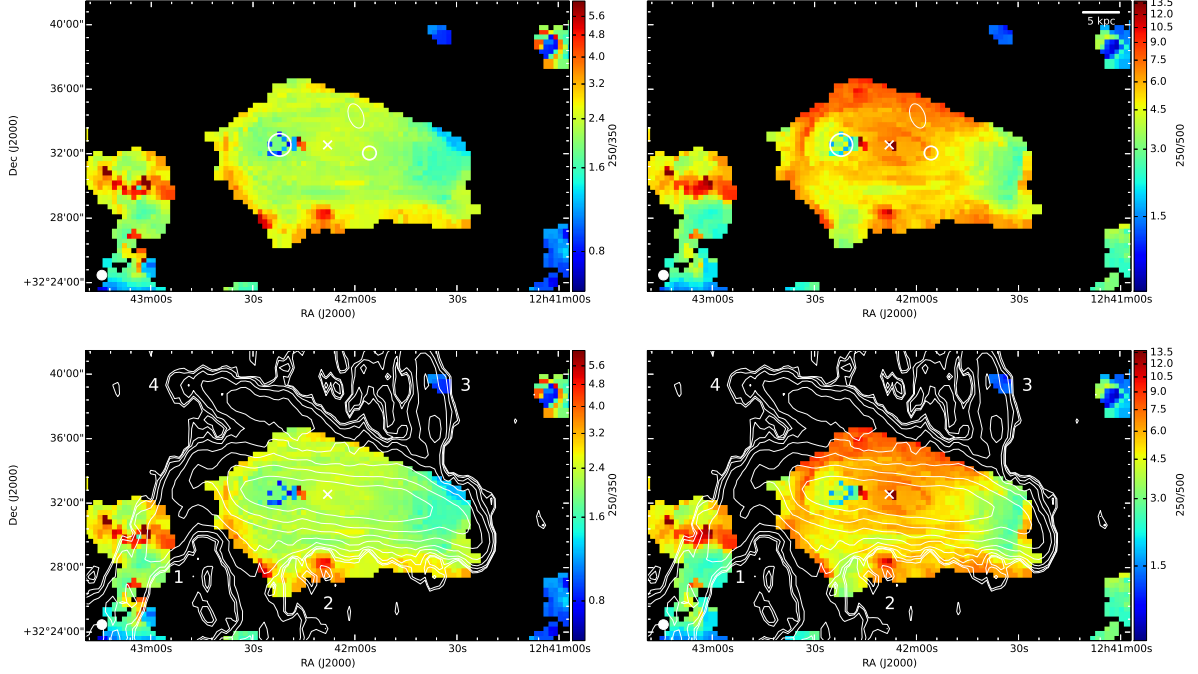


Fig. 9.— Left panels: the  $S_{250}/S_{350}$  ratio map derived from the adaptively smoothed SPIRE maps shown in Figure 5. Right panels: same as left panel but the  $S_{250}/S_{500}$  ratio map. The upper row shows the ratio maps at a pixel scale of  $18'' \text{ pixel}^{-1}$ . The lower rows compares these maps with the H I 21-cm emission (as contours) at a resolution  $45'' \times 87''$ . In column density units at the beam center, the contour levels are 0.5, 0.6, 0.8, 1.3, 2.6, 5.7, 12.9, 30.1 and  $70.7 \times 10^{20} \text{ cm}^{-2}$ . North is up and east to the left. The horizontal line in the upper right corner of the upper right panel represents 5 kpc. The white circles represent the approximate size of the H I supershells (Rand & van der Hulst 1993). The white ellipse indicates the position of the companion galaxy NGC 4627. The beam size at  $500 \mu\text{m}$  is indicated by a white filled circle in the bottom left corner of each panel. In all of the panels, the white “X” indicates the position of the infrared nucleus (Aaronson 1978, 1981).

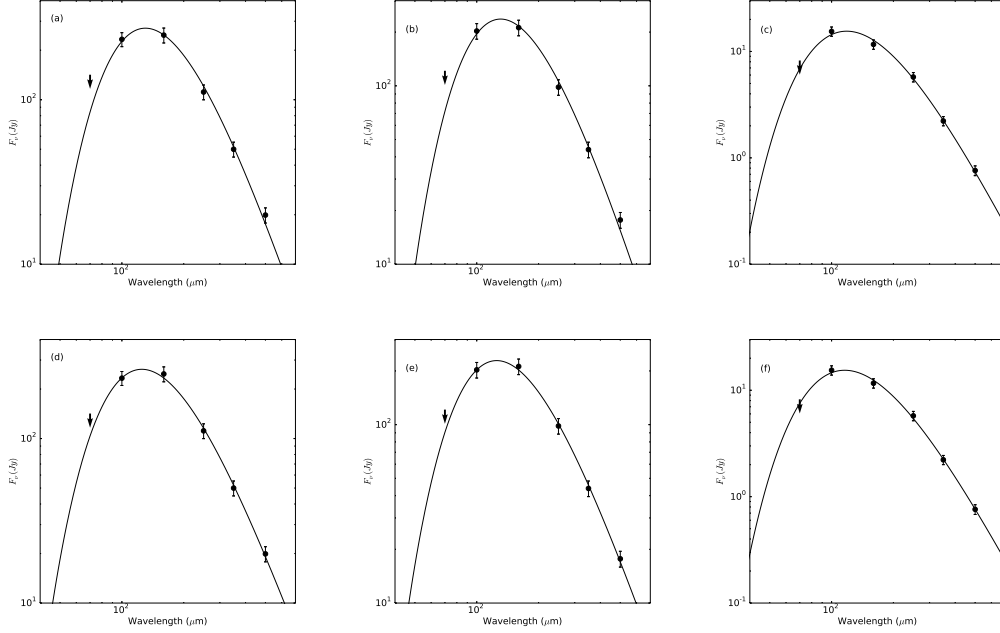


Fig. 10.— Single-temperature MBB fit to the global (panels a and d), disk (panels b and e), and superbubble (panels c and f) spectral energy distributions in the 70–500  $\mu\text{m}$  range. The upper panels show the fit with  $\beta = 2.0$  (panels a, b and c) whereas the lower panels show the fit with the spectral index  $\beta$  left as a free parameter (panels d, e and f). See Table 2 for details on the various fits.

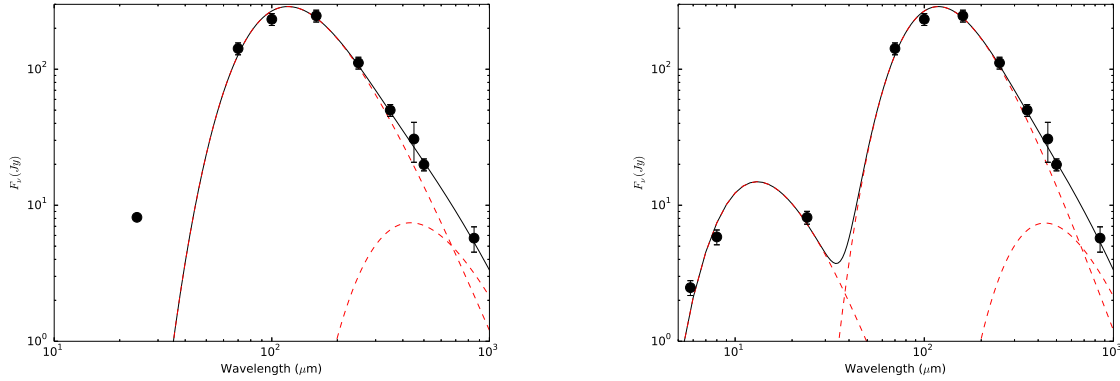


Fig. 11.— Left panel: Two-temperature MBB fit with  $\beta = 2.0$  (fixed) to the global spectral energy distribution. For the sake of comparison, we also show the flux density at 24  $\mu\text{m}$  (*Spitzer* MIPS, Dale et al. 2009). However, this data point was not included in the fit. Right panel: three-temperature MBB fit with  $\beta = 2.0$  (fixed) to the global spectral energy distribution. See Table 3 for the results from these fits.

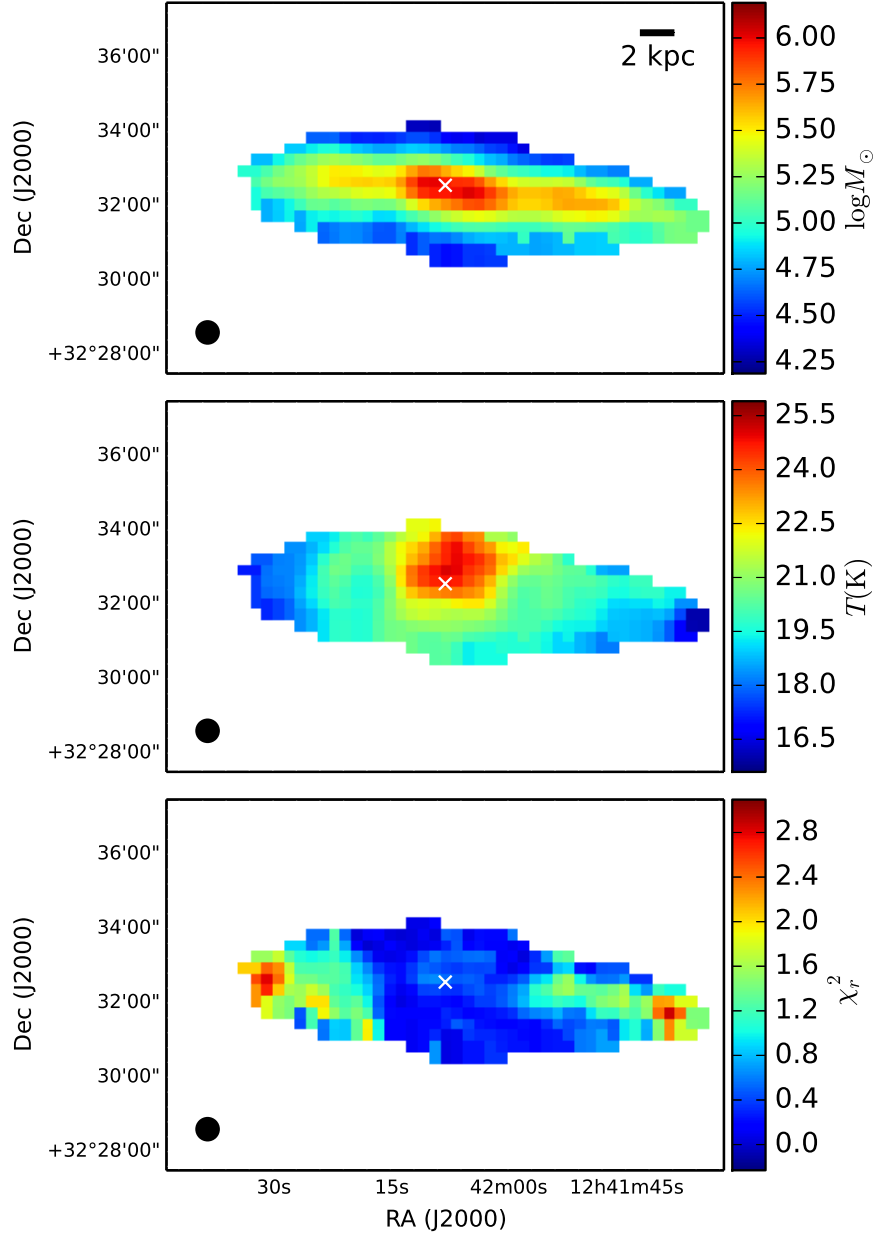


Fig. 12.— Pixel-by-pixel SED fits where the fluxes at 70-500  $\mu\text{m}$  from each pixel were fit with a single-temperature MBB with  $\beta = 2.0$  (fixed). Note that the 70  $\mu\text{m}$  flux is used as an upper limit, see text for detail. The pixel scale is  $18'' \text{ pixel}^{-1}$ . North is up and east is to the left. The horizontal line in the upper right corner of the upper panel represents 2 kpc. The beam size at 500  $\mu\text{m}$  is indicated by a black filled circle in the bottom left corner of each panel. In all of the panels, the white “X” indicates the position of the infrared nucleus (Aaronson 1978, 1981).

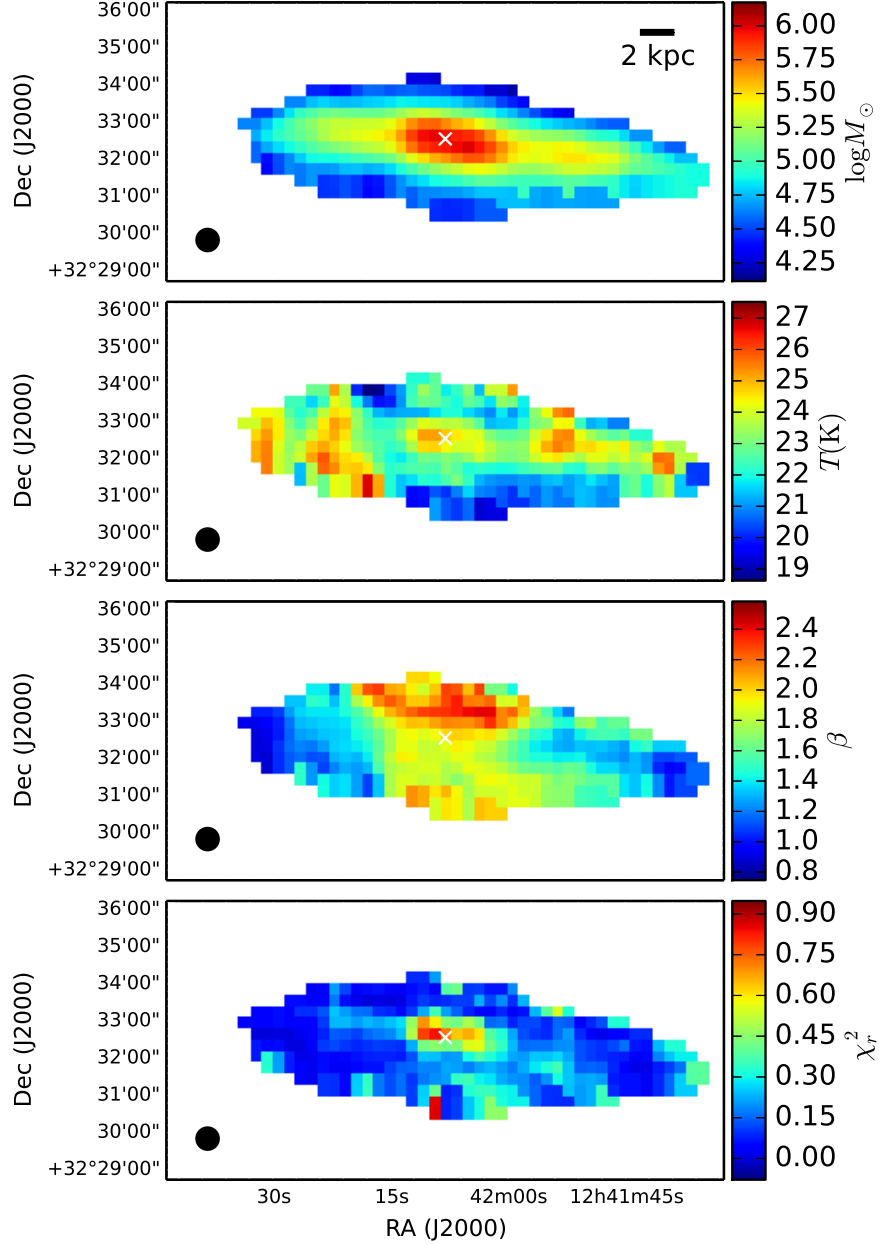


Fig. 13.— Same as Figure 12, except that  $\beta$  is now a free parameter. Note that the  $70\mu\text{m}$  flux is used as an upper limit, see text for detail. The pixel scale is  $18'' \text{ pixel}^{-1}$ . North is up and east is to the left. The horizontal line in the upper right corner of the upper panel represents 2 kpc. The beam size at  $500 \mu\text{m}$  is indicated by a black filled circle in the bottom left corner of each panel. In all of the panels, the white "X" indicates the position of the infrared nucleus (Aaronson 1978, 1981).

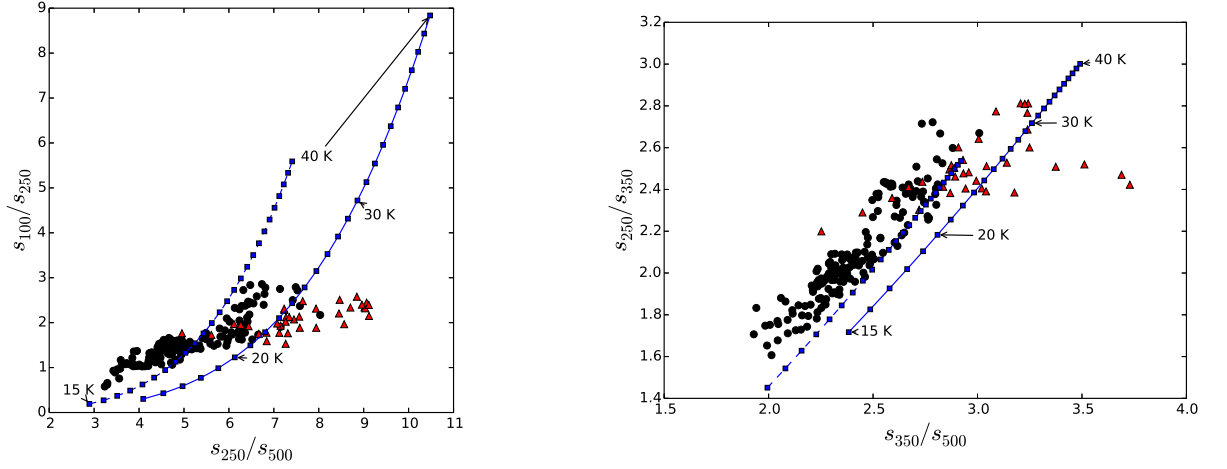


Fig. 14.— Left panel: PACS-SPIRE color-color diagram,  $S_{250}/S_{500}$  versus  $S_{100}/S_{250}$ , for each pixel in NGC 4631. Right panel: SPIRE color-color diagram,  $S_{250}/S_{350}$  versus  $S_{350}/S_{500}$  ratios, for each pixel in NGC 4631. The black circles represent the disk emission, whereas the red triangles represent emission in the superbubble region. See Figure 8 for the limits of the disk and superbubble regions. All of the images were convolved to the lower resolution of the SPIRE 500  $\mu\text{m}$  data (FWHM/2, 18'') before making this plot. For comparison, the expected relationship from a single modified blackbody with a dust emissivity of  $\beta = 2.0$  (*solid line*) and  $\beta = 1.5$  (*dashed line*) is also shown.

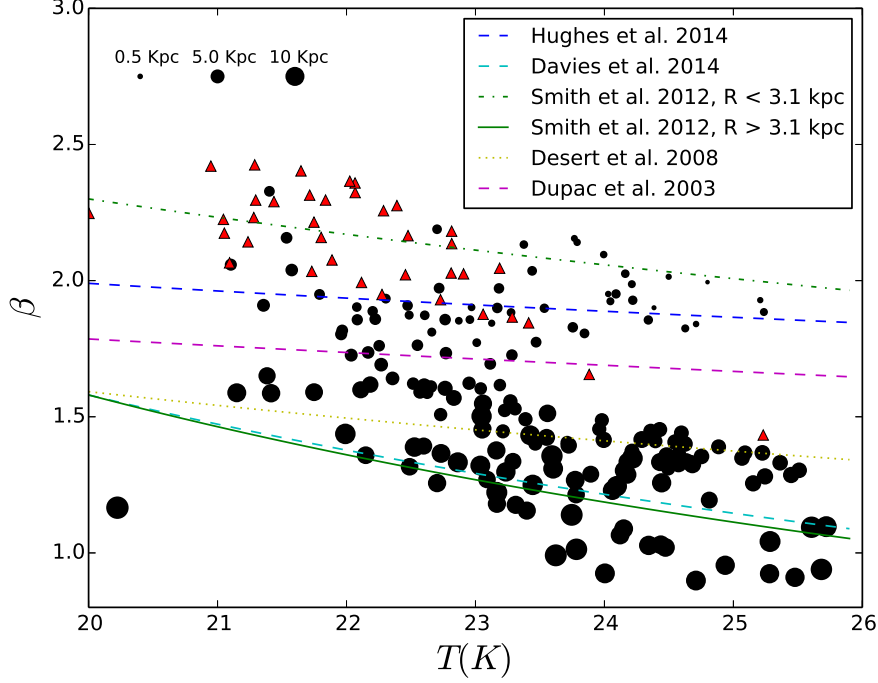


Fig. 15.— The observed anti-correlation between  $\beta$  and the dust temperature from the single-temperature MBB for the pixel-by-pixel SED fits. Symbols are the same as in Figure 14, except that the symbol size (diameter) for the disk measurements is now proportional to the radial distance from the center of the galaxy. The radial distance scale is shown in the upper left corner, where three different black circles are shown representing radial distances of 0.5, 5, and 10 kpc. We compared our data with the best fit of some of the  $\beta$ - $T$  relationships found in the literature: 1) resolved analysis of NGC 891 (dashed blue line, Hughes et al. 2014); 2) the *Herschel* Virgo Cluster Survey (dashed cyan line, Davies et al. 2014); 3) the green solid and dot-dashed lines represent the best  $\beta$ - $T$  fit from the resolved analysis of M31 (Smith et al. 2012) for a radial distance of  $3.1 < R < 15$  and  $R < 3.1$  kpc, respectively; 4) ARCHEOPS sources (yellow dotted line, Désert et al. 2008) and, 5) PRONAOS-based data for different regions of the ISM (Dupac et al. 2003).

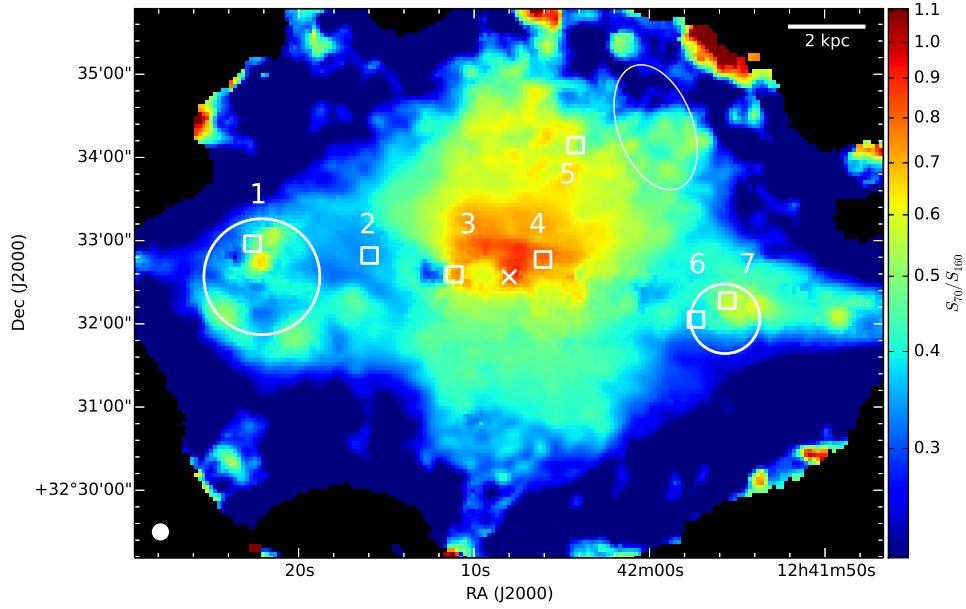


Fig. 16.— The  $S_{70}/S_{160}$  ratio map of the adaptively smoothed PACS maps shown in Figure 4. The open white squares mark the positions of the brightest X-ray point sources. The white dashed circles represent the approximate size of the H I supershells (Rand & van der Hulst 1993). The white ellipse indicates the position of the companion galaxy NGC 4627. The beam size at 160  $\mu$ m is indicated by a white filled circle in the bottom left corner. The white “X” indicates the position of the infrared nucleus (Aaronson 1978, 1981).

## REFERENCES

- Aaronson, M. 1978, *PASP*, 90, 28
- . 1981, *PASP*, 93, 535
- Alton, P. B., Davies, J. I., & Bianchi, S. 1999, *A&A*, 343, 51
- Aniano, G., Draine, B. T., Gordon, K. D., & Sandstrom, K. 2011, *PASP*, 123, 1218
- Bahcall, J. N. 1984, *ApJ*, 276, 169
- Bendo, G. J., Dale, D. A., Draine, B. T., Engelbracht, C. W., Kennicutt, Jr., R. C., Calzetti, D., Gordon, K. D., Helou, G., Hollenbach, D., Li, A., Murphy, E. J., Prescott, M. K. M., & Smith, J.-D. T. 2006, *ApJ*, 652, 283
- Bendo, G. J., Joseph, R. D., Wells, M., Gallais, P., Haas, M., Heras, A. M., Klaas, U., Laureijs, R. J., Leech, K., Lemke, D., Metcalfe, L., Rowan-Robinson, M., Schulz, B., & Telesco, C. 2003, *AJ*, 125, 2361
- Bianchi, S. 2013, *A&A*, 552, A89
- Bolatto, A. D., Warren, S. R., Leroy, A. K., Walter, F., Veilleux, S., Ostriker, E. C., Ott, J., Zwaan, M., Fisher, D. B., Weiss, A., Rosolowsky, E., & Hodge, J. 2013, *Nature*, 499, 450
- Bracco, A., Cooray, A., Veneziani, M., Amblard, A., Serra, P., Wardlow, J., Thompson, M. A., White, G., Auld, R., Baes, M., Bertoldi, F., Buttiglione, S., Cava, A., Clements, D. L., Dariush, A., de Zotti, G., Dunne, L., Dye, S., Eales, S., Fritz, J., Gomez, H., Hopwood, R., Ibar, I., Ivison, R. J., Jarvis, M., Lagache, G., Lee, M. G., Leeuw, L., Maddox, S., Michałowski, M., Pearson, C., Pohlen, M., Rigby, E., Rodighiero, G., Smith, D. J. B., Temi, P., Vaccari, M., & van der Werf, P. 2011, *MNRAS*, 412, 1151
- Braine, J., Kruegel, E., Sievers, A., & Wielebinski, R. 1995, *A&A*, 295, L55
- Calzetti, D., Wu, S.-Y., Hong, S., Kennicutt, R. C., Lee, J. C., Dale, D. A., Engelbracht, C. W., van Zee, L., Draine, B. T., Hao, C.-N., Gordon, K. D., Moustakas, J., Murphy, E. J., Regan, M., Begum, A., Block, M., Dalcanton, J., Funes, J., Gil de Paz, A., Johnson, B., Sakai, S., Skillman, E., Walter, F., Weisz, D., Williams, B., & Wu, Y. 2010, *ApJ*, 714, 1256
- Carpano, S., Pollock, A. M. T., King, A. R., Wilms, J., & Ehle, M. 2007, *A&A*, 471, L55
- Cicone, C., Maiolino, R., Sturm, E., Graciá-Carpio, J., Feruglio, C., Neri, R., Aalto, S., Davies, R., Fiore, F., Fischer, J., García-Burillo, S., González-Alfonso, E., Hailey-Dunsheath, S., Piconcelli, E., & Veilleux, S. 2014, *A&A*, 562, A21
- Combes, F. 1978, *A&A*, 65, 47



- Cooper, J. L., Bicknell, G. V., Sutherland, R. S., & Bland-Hawthorn, J. 2008, *ApJ*, 674, 157
- Coupeaud, A., Demyk, K., Meny, C., Nayral, C., Delpech, F., Leroux, H., Depecker, C., Creff, G., Brubach, J.-B., & Roy, P. 2011, *A&A*, 535, A124
- Crillon, R., & Monnet, G. 1969, *A&A*, 2, 1
- Dale, D. A., Aniano, G., Engelbracht, C. W., Hinz, J. L., Krause, O., Montiel, E. J., Roussel, H., Appleton, P. N., Armus, L., Beirão, P., Bolatto, A. D., Brandl, B. R., Calzetti, D., Crocker, A. F., Croxall, K. V., Draine, B. T., Galametz, M., Gordon, K. D., Groves, B. A., Hao, C.-N., Helou, G., Hunt, L. K., Johnson, B. D., Kennicutt, R. C., Koda, J., Leroy, A. K., Li, Y., Meidt, S. E., Miller, A. E., Murphy, E. J., Rahman, N., Rix, H.-W., Sandstrom, K. M., Sauvage, M., Schinnerer, E., Skibba, R. A., Smith, J.-D. T., Tabatabaei, F. S., Walter, F., Wilson, C. D., Wolfire, M. G., & Zibetti, S. 2012, *ApJ*, 745, 95
- Dale, D. A., Bendo, G. J., Engelbracht, C. W., Gordon, K. D., Regan, M. W., Armus, L., Cannon, J. M., Calzetti, D., Draine, B. T., Helou, G., Joseph, R. D., Kennicutt, R. C., Li, A., Murphy, E. J., Roussel, H., Walter, F., Hanson, H. M., Hollenbach, D. J., Jarrett, T. H., Kewley, L. J., Lamanna, C. A., Leitherer, C., Meyer, M. J., Rieke, G. H., Rieke, M. J., Sheth, K., Smith, J. D. T., & Thornley, M. D. 2005, *ApJ*, 633, 857
- Dale, D. A., Cohen, S. A., Johnson, L. C., Schuster, M. D., Calzetti, D., Engelbracht, C. W., Gil de Paz, A., Kennicutt, R. C., Lee, J. C., Begum, A., Block, M., Dalcanton, J. J., Funes, J. G., Gordon, K. D., Johnson, B. D., Marble, A. R., Sakai, S., Skillman, E. D., van Zee, L., Walter, F., Weisz, D. R., Williams, B., Wu, S.-Y., & Wu, Y. 2009, *ApJ*, 703, 517
- Dale, D. A., Gil de Paz, A., Gordon, K. D., Hanson, H. M., Armus, L., Bendo, G. J., Bianchi, L., Block, M., Boissier, S., Boselli, A., Buckalew, B. A., Buat, V., Burgarella, D., Calzetti, D., Cannon, J. M., Engelbracht, C. W., Helou, G., Hollenbach, D. J., Jarrett, T. H., Kennicutt, R. C., Leitherer, C., Li, A., Madore, B. F., Martin, D. C., Meyer, M. J., Murphy, E. J., Regan, M. W., Roussel, H., Smith, J. D. T., Sosey, M. L., Thilker, D. A., & Walter, F. 2007, *ApJ*, 655, 863
- Davies, J. I., Bianchi, S., Baes, M., Bendo, G. J., Clemens, M., De Looze, I., Alighieri, S. d. S., Fritz, J., Fuller, C., Pappalardo, C., Hughes, T. M., Madden, S., Smith, M. W. L., Verstappen, J., & Vlahakis, C. 2014, *MNRAS*, 438, 1922
- Désert, F.-X., Macías-Pérez, J. F., Mayet, F., Giardino, G., Renault, C., Aumont, J., Benoît, A., Bernard, J.-P., Ponthieu, N., & Tristram, M. 2008, *A&A*, 481, 411
- Donahue, M., Aldering, G., & Stocke, J. T. 1995, *ApJ*, 450, L45
- Draine, B. T. 2003, *ARA&A*, 41, 241

- Draine, B. T., Dale, D. A., Bendo, G., Gordon, K. D., Smith, J. D. T., Armus, L., Engelbracht, C. W., Helou, G., Kennicutt, Jr., R. C., Li, A., Roussel, H., Walter, F., Calzetti, D., Moustakas, J., Murphy, E. J., Rieke, G. H., Bot, C., Hollenbach, D. J., Sheth, K., & Teplitz, H. I. 2007, *ApJ*, 663, 866
- Draine, B. T., & Li, A. 2007, *ApJ*, 657, 810
- Dumke, M., Krause, M., & Wielebinski, R. 2004, *A&A*, 414, 475
- Dumke, M., Nieten, C., Thuma, G., Wielebinski, R., & Walsh, W. 2001, *A&A*, 373, 853
- Dupac, X., Bernard, J.-P., Boudet, N., Giard, M., Lamarre, J.-M., Mény, C., Pajot, F., Ristorcelli, I., Serra, G., Stepnik, B., & Torre, J.-P. 2003, *A&A*, 404, L11
- Ekers, R. D., & Sancisi, R. 1977, *A&A*, 54, 973
- Fabbiano, G., & Trinchieri, G. 1987, *ApJ*, 315, 46
- Golla, G., Dettmar, R.-J., & Domgoergen, H. 1996, *A&A*, 313, 439
- Golla, G., & Hummel, E. 1994, *A&A*, 284, 777
- Golla, G., & Wielebinski, R. 1994, *A&A*, 286, 733
- Griffin, M. J., Abergel, A., Abreu, A., Ade, P. A. R., André, P., Augueres, J.-L., Babbedge, T., Bae, Y., Baillie, T., Baluteau, J.-P., Barlow, M. J., Bendo, G., Benielli, D., Bock, J. J., Bonhomme, P., Brisbin, D., Brockley-Blatt, C., Caldwell, M., Cara, C., Castro-Rodriguez, N., Cerulli, R., Chaniel, P., Chen, S., Clark, E., Clements, D. L., Clerc, L., Coker, J., Communal, D., Conversi, L., Cox, P., Crumb, D., Cunningham, C., Daly, F., Davis, G. R., de Antoni, P., Delderfield, J., Devin, N., di Giorgio, A., Didschuns, I., Dohlen, K., Donati, M., Dowell, A., Dowell, C. D., Duband, L., Dumaye, L., Emery, R. J., Ferlet, M., Ferrand, D., Fontignie, J., Fox, M., Franceschini, A., Frerking, M., Fulton, T., Garcia, J., Gastaud, R., Gear, W. K., Glenn, J., Goizel, A., Griffin, D. K., Grundy, T., Guest, S., Guillemet, L., Hargrave, P. C., Harwit, M., Hastings, P., Hatziminaoglou, E., Herman, M., Hinde, B., Hristov, V., Huang, M., Imhof, P., Isaak, K. J., Israelsson, U., Ivison, R. J., Jennings, D., Kiernan, B., King, K. J., Lange, A. E., Latter, W., Laurent, G., Laurent, P., Leeks, S. J., Lellouch, E., Levenson, L., Li, B., Li, J., Lilienthal, J., Lim, T., Liu, S. J., Lu, N., Madden, S., Mainetti, G., Marliani, P., McKay, D., Mercier, K., Molinari, S., Morris, H., Moseley, H., Mulder, J., Mur, M., Naylor, D. A., Nguyen, H., O’Halloran, B., Oliver, S., Olofsson, G., Olofsson, H.-G., Orfei, R., Page, M. J., Pain, I., Panuzzo, P., Papageorgiou, A., Parks, G., Parr-Burman, P., Pearce, A., Pearson, C., Pérez-Fournon, I., Pinsard, F., Pisano, G., Podosek, J., Pohlen, M., Polehampton, E. T., Pouliquen, D., Rigopoulou, D., Rizzo, D., Roseboom, I. G., Roussel, H., Rowan-Robinson, M., Rownd, B., Saraceno, P., Sauvage, M., Savage, R., Savini, G., Sawyer, E., Scharnberg, C., Schmitt, D., Schneider, N., Schulz, B., Schwartz, A., Shafer, R., Shupe, D. L., Sibthorpe, B., Sidher, S., Smith, A., Smith, A. J.,

- Smith, D., Spencer, L., Stobie, B., Sudiwala, R., Sukhatme, K., Surace, C., Stevens, J. A., Swinyard, B. M., Trichas, M., Tourette, T., Triou, H., Tseng, S., Tucker, C., Turner, A., Vaccari, M., Valtchanov, I., Vigroux, L., Virique, E., Voellmer, G., Walker, H., Ward, R., Waskett, T., Weilert, M., Wesson, R., White, G. J., Whitehouse, N., Wilson, C. D., Winter, B., Woodcraft, A. L., Wright, G. S., Xu, C. K., Zavagno, A., Zemcov, M., Zhang, L., & Zonca, E. 2010, *A&A*, 518, L3
- Hoopes, C. G., Walterbos, R. A. M., & Rand, R. J. 1999, *ApJ*, 522, 669
- Howk, J. C., & Savage, B. D. 1997, *AJ*, 114, 2463
- Hughes, T. M., Baes, M., Fritz, J., Smith, M. W. L., Parkin, T. J., Gentile, G., Bendo, G. J., Wilson, C. D., Allaert, F., Bianchi, S., De Looze, I., Verstappen, J., Viaene, S., Boquien, M., Boselli, A., Clements, D. L., Davies, J. I., Galametz, M., Madden, S. C., Rémy-Ruyer, A., & Spinoglio, L. 2014, *A&A*, 565, A4
- Hummel, E., Beck, R., & Dahlem, M. 1991, *A&A*, 248, 23
- Hummel, E., & Dettmar, R.-J. 1990, *A&A*, 236, 33
- Hummel, E., Lesch, H., Wielebinski, R., & Schlickeiser, R. 1988, *A&A*, 197, L29
- Irwin, J., Beck, R., Benjamin, R. A., Dettmar, R.-J., English, J., Heald, G., Henriksen, R. N., Johnson, M., Krause, M., Li, J.-T., Miskolczi, A., Mora, S. C., Murphy, E. J., Oosterloo, T., Porter, T. A., Rand, R. J., Saikia, D. J., Schmidt, P., Strong, A. W., Walterbos, R., Wang, Q. D., & Wiegert, T. 2012, *AJ*, 144, 44
- Irwin, J. A., Wilson, C. D., Wiegert, T., Bendo, G. J., Warren, B. E., Wang, Q. D., Israel, F. P., Serjeant, S., Knapen, J. H., Brinks, E., Tilanus, R. P. J., van der Werf, P., & Mühle, S. 2011, *MNRAS*, 410, 1423
- Israel, F. P. 2009, *A&A*, 506, 689
- Jurac, S., Johnson, R. E., & Donn, B. 1998, *ApJ*, 503, 247
- Kelly, B. C., Shetty, R., Stutz, A. M., Kauffmann, J., Goodman, A. A., & Launhardt, R. 2012, *ApJ*, 752, 55
- Kennicutt, R. C., & Evans, N. J. 2012, *ARA&A*, 50, 531
- Kennicutt, Jr., R. C. 1998, *ARA&A*, 36, 189
- Kennicutt, Jr., R. C., Hao, C.-N., Calzetti, D., Moustakas, J., Dale, D. A., Bendo, G., Engelbracht, C. W., Johnson, B. D., & Lee, J. C. 2009, *ApJ*, 703, 1672
- Lynds, C. R., & Sandage, A. R. 1963, *ApJ*, 137, 1005

- Martin, C., & Kern, B. 2001, *ApJ*, 555, 258
- McCormick, A., Veilleux, S., & Rupke, D. S. N. 2013, *ApJ*, 774, 126
- Meléndez, M., Mushotzky, R. F., Shimizu, T. T., Barger, A. J., & Cowie, L. L. 2014, *ApJ*, 794, 152
- Meny, C., Gromov, V., Boudet, N., Bernard, J.-P., Paradis, D., & Nayral, C. 2007, *A&A*, 468, 171
- Mora, S. C., & Krause, M. 2013, *A&A*, 560, A42
- Neininger, N., & Dumke, M. 1999, *Proceedings of the National Academy of Science*, 96, 5360
- Ott, S. 2010, in *Astronomical Society of the Pacific Conference Series*, Vol. 434, *Astronomical Data Analysis Software and Systems XIX*, ed. Y. Mizumoto, K.-I. Morita, & M. Ohishi, 139
- Paradis, D., Veneziani, M., Noriega-Crespo, A., Paladini, R., Piacentini, F., Bernard, J. P., de Bernardis, P., Calzoletti, L., Faustini, F., Martin, P., Masi, S., Montier, L., Natoli, P., Ristorcelli, I., Thompson, M. A., Traficante, A., & Molinari, S. 2010, *A&A*, 520, L8
- Pilbratt, G. L., Riedinger, J. R., Passvogel, T., Crone, G., Doyle, D., Gageur, U., Heras, A. M., Jewell, C., Metcalfe, L., Ott, S., & Schmidt, M. 2010, *A&A*, 518, L1
- Poglitsch, A., Waelkens, C., Geis, N., Feuchtgruber, H., Vandenbussche, B., Rodriguez, L., Krause, O., Renotte, E., van Hoof, C., Saraceno, P., Cepa, J., Kerschbaum, F., Agnèse, P., Ali, B., Altieri, B., Andreani, P., Augueres, J.-L., Balog, Z., Barl, L., Bauer, O. H., Belbachir, N., Benedettini, M., Billot, N., Boulade, O., Bischof, H., Blommaert, J., Callut, E., Cara, C., Cerulli, R., Cesarsky, D., Contursi, A., Creten, Y., De Meester, W., Doublier, V., Doumayrou, E., Duband, L., Exter, K., Genzel, R., Gillis, J.-M., Grözinger, U., Henning, T., Herreros, J., Huygen, R., Inguscio, M., Jakob, G., Jamar, C., Jean, C., de Jong, J., Katterloher, R., Kiss, C., Klaas, U., Lemke, D., Lutz, D., Madden, S., Marquet, B., Martignac, J., Mazy, A., Merken, P., Montfort, F., Morbidelli, L., Müller, T., Nielbock, M., Okumura, K., Orfei, R., Ottensamer, R., Pezzuto, S., Popesso, P., Putzeys, J., Regibo, S., Reveret, V., Royer, P., Sauvage, M., Schreiber, J., Stegmaier, J., Schmitt, D., Schubert, J., Sturm, E., Thiel, M., Tofani, G., Vavrek, R., Wetzstein, M., Wieprecht, E., & Wiezorrek, E. 2010, *A&A*, 518, L2
- Radburn-Smith, D. J., de Jong, R. S., Seth, A. C., Bailin, J., Bell, E. F., Brown, T. M., Bullock, J. S., Courteau, S., Dalcanton, J. J., Ferguson, H. C., Goudfrooij, P., Holfeltz, S., Holwerda, B. W., Purcell, C., Sick, J., Streich, D., Vljajic, M., & Zucker, D. B. 2011, *ApJS*, 195, 18
- Rand, R. J. 1994, *A&A*, 285, 833
- . 2000, *ApJ*, 535, 663
- Rand, R. J., Kulkarni, S. R., & Hester, J. J. 1992, *ApJ*, 396, 97

- Rand, R. J., & Stone, J. M. 1996, *AJ*, 111, 190
- Rand, R. J., & van der Hulst, J. M. 1993, *AJ*, 105, 2098
- Raymond, J. C., Ghavamian, P., Williams, B. J., Blair, W. P., Borkowski, K. J., Gaetz, T. J., & Sankrit, R. 2013, *ApJ*, 778, 161
- Read, A. M., Ponman, T. J., & Strickland, D. K. 1997, *MNRAS*, 286, 626
- Rice, W., Lonsdale, C. J., Soifer, B. T., Neugebauer, G., Kopan, E. L., Lloyd, L. A., de Jong, T., & Habing, H. J. 1988, *ApJS*, 68, 91
- Roberts, M. S. 1968, *ApJ*, 151, 117
- Roussel, H. 2013, *PASP*, 125, 1126
- Roussel, H., Wilson, C. D., Vigroux, L., Isaak, K. G., Sauvage, M., Madden, S. C., Auld, R., Baes, M., Barlow, M. J., Bendo, G. J., Bock, J. J., Boselli, A., Bradford, M., Buat, V., Castro-Rodriguez, N., Chanical, P., Charlot, S., Ciesla, L., Clements, D. L., Cooray, A., Cormier, D., Cortese, L., Davies, J. I., Dwek, E., Eales, S. A., Elbaz, D., Galametz, M., Galliano, F., Gear, W. K., Glenn, J., Gomez, H. L., Griffin, M., Hony, S., Levenson, L. R., Lu, N., O’Halloran, B., Okumura, K., Oliver, S., Page, M. J., Panuzzo, P., Papageorgiou, A., Parkin, T. J., Perez-Fournon, I., Pohlen, M., Rangwala, N., Rigby, E. E., Rykala, A., Sacchi, N., Schulz, B., Schirm, M. R. P., Smith, M. W. L., Spinoglio, L., Stevens, J. A., Srinivasan, S., Symeonidis, M., Trichas, M., Vaccari, M., Wozniak, H., Wright, G. S., & Zeilinger, W. W. 2010, *A&A*, 518, L66
- Schechtman-Rook, A., & Hess, K. M. 2012, *ApJ*, 750, 171
- Seth, A. C., Dalcanton, J. J., & de Jong, R. S. 2005a, *AJ*, 129, 1331
- . 2005b, *AJ*, 130, 1574
- Shetty, R., Kauffmann, J., Schnee, S., & Goodman, A. A. 2009a, *ApJ*, 696, 676
- Shetty, R., Kauffmann, J., Schnee, S., Goodman, A. A., & Ercolano, B. 2009b, *ApJ*, 696, 2234
- Skibba, R. A., Engelbracht, C. W., Dale, D., Hinz, J., Zibetti, S., Crocker, A., Groves, B., Hunt, L., Johnson, B. D., Meidt, S., Murphy, E., Appleton, P., Armus, L., Bolatto, A., Brandl, B., Calzetti, D., Croxall, K., Galametz, M., Gordon, K. D., Kennicutt, R. C., Koda, J., Krause, O., Montiel, E., Rix, H.-W., Roussel, H., Sandstrom, K., Sauvage, M., Schinnerer, E., Smith, J. D., Walter, F., Wilson, C. D., & Wolfire, M. 2011, *ApJ*, 738, 89
- Smith, A. M., Collins, N. R., Waller, W. H., Roberts, M. S., Smith, D. A., Bohlin, R. C., Cheng, K.-P., Fanelli, M. N., Neff, S. G., O’Connell, R. W., Parise, R. A., Smith, E. P., & Stecher, T. P. 2001, *ApJ*, 546, 829

- Smith, M. W. L., Eales, S. A., Gomez, H. L., Roman-Duval, J., Fritz, J., Braun, R., Baes, M., Bendo, G. J., Blommaert, J. A. D. L., Boquien, M., Boselli, A., Clements, D. L., Cooray, A. R., Cortese, L., de Looze, I., Ford, G. P., Gear, W. K., Gentile, G., Gordon, K. D., Kirk, J., Lebouteiller, V., Madden, S., Mentuch, E., O’Halloran, B., Page, M. J., Schulz, B., Spinoglio, L., Verstappen, J., Wilson, C. D., & Thilker, D. A. 2012, *ApJ*, 756, 40
- Soria, R., & Ghosh, K. K. 2009, *ApJ*, 696, 287
- Stevens, J. A., Amure, M., & Gear, W. K. 2005, *MNRAS*, 357, 361
- Strickland, D. K., Heckman, T. M., Colbert, E. J. M., Hoopes, C. G., & Weaver, K. A. 2004, *ApJS*, 151, 193
- Sturm, E., González-Alfonso, E., Veilleux, S., Fischer, J., Graciá-Carpio, J., Hailey-Dunsheath, S., Contursi, A., Poglitsch, A., Sternberg, A., Davies, R., Genzel, R., Lutz, D., Tacconi, L., Verma, A., Maiolino, R., & de Jong, J. A. 2011, *ApJ*, 733, L16
- Taylor, C. L., & Wang, Q. D. 2003, *AJ*, 125, 1204
- Tüllmann, R., Breitschwerdt, D., Rossa, J., Pietsch, W., & Dettmar, R.-J. 2006a, *A&A*, 457, 779
- Tüllmann, R., Pietsch, W., Rossa, J., Breitschwerdt, D., & Dettmar, R.-J. 2006b, *A&A*, 448, 43
- van der Kruit, P. C. 1988, *A&A*, 192, 117
- Veilleux, S., Cecil, G., & Bland-Hawthorn, J. 2005, *ARA&A*, 43, 769
- Veilleux, S., Meléndez, M., Sturm, E., Gracia-Carpio, J., Fischer, J., González-Alfonso, E., Contursi, A., Lutz, D., Poglitsch, A., Davies, R., Genzel, R., Tacconi, L., de Jong, J. A., Sternberg, A., Netzer, H., Hailey-Dunsheath, S., Verma, A., Rupke, D. S. N., Maiolino, R., Teng, S. H., & Polisensky, E. 2013, *ApJ*, 776, 27
- Veneziani, M., Ade, P. A. R., Bock, J. J., Boscaleri, A., Crill, B. P., de Bernardis, P., De Gasperis, G., de Oliveira-Costa, A., De Troia, G., Di Stefano, G., Ganga, K. M., Jones, W. C., Kisner, T. S., Lange, A. E., MacTavish, C. J., Masi, S., Mauskopf, P. D., Montroy, T. E., Natoli, P., Netterfield, C. B., Pascale, E., Piacentini, F., Pietrobon, D., Polenta, G., Ricciardi, S., Romeo, G., & Ruhl, J. E. 2010, *ApJ*, 713, 959
- Vogler, A., & Pietsch, W. 1996, *A&A*, 311, 35
- Wang, Q. D., Immler, S., Walterbos, R., Lauroesch, J. T., & Breitschwerdt, D. 2001, *ApJ*, 555, L99
- Wang, Q. D., Walterbos, R. A. M., Steakley, M. F., Norman, C. A., & Braun, R. 1995, *ApJ*, 439, 176
- Weliachew, L., Sancisi, R., & Guélin, M. 1978, *A&A*, 65, 37

- Winter, L. M., Mushotzky, R. F., & Reynolds, C. S. 2006, *ApJ*, 649, 730
- . 2007, *ApJ*, 655, 163
- Yamasaki, N. Y., Sato, K., Mitsuishi, I., & Ohashi, T. 2009, *PASJ*, 61, 291
- Young, J. S., Xie, S., Kenney, J. D. P., & Rice, W. L. 1989, *ApJS*, 70, 699
- Ysard, N., Juvela, M., Demyk, K., Guillet, V., Abergel, A., Bernard, J.-P., Malinen, J., Mény, C., Montier, L., Paradis, D., Ristorcelli, I., & Verstraete, L. 2012, *A&A*, 542, A21
- Zibetti, S. 2009, ArXiv e-prints
- Zibetti, S., Charlot, S., & Rix, H.-W. 2009, *MNRAS*, 400, 1181